Ultrafast multiple paramagnetic species EPR imaging using a total variation based model

Mehdi Boussâa[a,b], Rémy Abergel[a], Sylvain Durand[a], Yves-Michel Frapart[b]

[a] *Université Paris Cité, CNRS, MAP5, F-75006 Paris, France*
[b] *Université Paris Cité, CNRS, LCBPT, F-75006 Paris, France*

Abstract

An EPR spectrum or an EPR sinogram for imaging contains information about all the paramagnetic species that are in the analyzed sample. When only one species is present, an image of its spatial repartition can be reconstructed from the sinogram by using the well-known Filtered Back-Projection (FBP). However, in the case of several species, the FBP does not allow the reconstruction of the images of each species from a standard acquisition. One has to use for this spectral-spatial imaging whose acquisition can be very long. A new approach, based on Total Variation minimization, is proposed in order to efficiently extract the spatial repartitions of all the species present in a sample from standard imaging data and therefore drastically reduce the acquisition time. Experiments have been carried out on Tetrathiatriarylmethyl, nitroxide and DPPH.

Keywords: EPR source separation, EPR imaging, variational models, total variation

1. Introduction

Electron Paramagnetic Resonance Imaging (EPRI) and spectroscopy are now regarded as unique, noninvasive and versatile approaches for locating, characterizing and possibly quantifying paramagnetic species. Nowadays, EPR imaging seems to have potential applications in many kinds of scientific fields, such as in biomedical sciences [1–4], Li-ion batteries [5] and detection of defects on material surface [6, 7]. Thus, the detection and measurement of paramagnetic species is crucial for the development of new materials, new diagnostic methods and treatment perspectives. An EPRI acquisition is recorded like an EPR spectrum, but using an additional magnetic field

gradient in a set of different orientations around the sample. The acquisition can be expressed as a convolution of the EPR spectrum shape with the species quantity along the axis of the gradient (namely the convolution with the Radon transform of the species quantity). A post-processing step is needed to obtain an image of the species repartition from the acquired spectra. The classical Filter Back-Projection (FBP) is implemented in commercial spectrometers. This direct two-step method consists in a filtering (more precisely, a deconvolution) followed by a back-projection. However, inverse one-step methods are known to better prevent artifacts occurrence. In particular, recent publications suggest using a variational method based on Total Variation (TV) [8–10] as it allows recovering noiseless images, with sharp edges, from a reduced number of projections. An online usable algorithm was recently published [11].

Intrinsically, an EPR spectrum and therefore an EPR image contain all the paramagnetic species that are observable within the sample, typically the various radicals present in the sample (for instance, using nitrones spin traps will lead to the observation of both superoxide and hydroxyl adduct at the same time). To obtain images of the different species therein, spectral-spatial imaging can be used [6, 12, 13]. Such experiment is extremely long, especially in common commercial EPR imagers. This has led to several strategies such as hardware developpement [14] or data acquisition optimisation [15] being developped.

Using a TV-based variationnal method to post process acquired data opens up new perspectives since, by exploiting correlations between neighboring voxels on the reconstructed images, this method allows efficient separation of multiple source images from reduced data. This article reports a new approach to obtain the images of several paramagnetic species without acquiring a spectral spatial image, but only standard imaging data. It consists, first, in extracting the EPR spectrum of each species from the acquired spectrum. Then, these spectra are used, with the acquired sinogram, to reconstruct the images of the different species using TV-regularized least-squares. Unlike other methods, it does not need to separate the spectra of the species at each voxel. Moreover, it requires mainly one easy-to-handle parameter, and it is implemented in an $\mathrm{O}(N \log N)$ iterative algorithm which allows $3D$-images to be processed in a reasonable amount of time. The proposed method has been evaluated on paramagnetic species presenting very different spectrum shapes (Tetrathiatriarylmethyl and nitroxide), and pretty similar shapes (Tetrathiatriarylmethyl and DPPH). This opens the way to

faster EPR imaging by a couple of orders of magnitude, and new applications in any domain dealing with paramagnetic species such as biology, materials and chemistry.

2. Modeling and discretization of EPR measurements

2.1. Continuous acquisition model

When a sample containing a paramagnetic species X is placed in the resonance cavity of an EPR spectrometer, it generates a signal which is called a spectrum and can be modeled as a function $h_X : \mathbb{R}_+ \to \mathbb{R}$ satisfying

$$\forall B \in \mathbb{R}_+, \quad h_X(B) = Q_X \, h_X^{\mathrm{ref}}(B)\,, \tag{1}$$

where B denotes the intensity of the homogeneous magnetic field applied to cavity, Q_X denotes the total amount of species X placed in the resonator and h_X^{ref} denotes the reference spectrum of X. The latter can be viewed, for a set of acquisition parameters, as the EPR signature of the paramagnetic species X in its molecular environment.

As can be observed in (1), the measured spectrum is not dependent of the spatial repartition of the species X within the cavity of the instrument. Therefore, no spatial information is embedded in such kind of measurement. To perform EPR imaging, that is, the reconstruction of the spatial repartition of X, some spatialization of the measurements is needed. This is usually achieved using magnetic gradient coils that generate an additional field gradient with intensity varying linearly along a given direction. Denoting by $U_X : \mathbb{R}^3 \to \mathbb{R}$ the spatial repartition of the species X, by $e_{(\theta,\varphi)} = (\cos\theta \sin\varphi, \sin\theta \sin\varphi, \cos\varphi)$ the direction of the field gradient parameterized by two angles $\theta \in [0, 2\pi]$ and $\varphi \in [0, \pi]$ in a spherical coordinate system, and denoting by μ the field gradient intensity, the acquired signal S_X^μ satisfies, for all $(B, \theta, \varphi) \in \mathbb{R}_+ \times [0, 2\pi] \times [0, \pi]$,

$$S_X^\mu(B, \theta, \varphi) = \int_{\mathbb{R}^3} U_X(x) \, h_X\left(B + \left\langle \mu e_{(\theta,\varphi)}, x \right\rangle\right) dx\,, \tag{2}$$

where $\langle \cdot, \cdot \rangle$ denotes the Euclidean inner product in $\mathbb{R}^3$. The signal S_X^μ is called a sinogram and, for a given field gradient direction (θ, φ), the monodimensional signal $B \mapsto S_X^\mu(B, \theta, \varphi)$ is called a projection. It has been known

for a long time that (2) can be reformulated using the Radon transform operator [16–18]. Indeed, for all $(B, \theta, \varphi) \in \mathbb{R}_+ \times [0, 2\pi] \times [0, \pi]$, one can show that

$$S_X^\mu(B, \theta, \varphi) = \left(h_X^\mu * \mathcal{R}_{\theta,\varphi}(U_X)\right)(-B/\mu)\,, \tag{3}$$

where $h_X^\mu : s \mapsto h_X(-s/\mu)$ represents a dilatation by factor $-\mu$ of the spectrum of X, $\mathcal{R}_{(\theta,\varphi)}(U_X)$ is the Radon transform of U_X in the direction (θ, φ) and $*$ denotes the convolution operator (see [11] for the explicit definitions). Equation (3) explicitly highlights the relationship between the measured sinogram S_X^μ and the quantity of interest U_X. The reconstruction of U_X from S_X^μ is called an *inverse problem* and modern ways to address it are based on variational approaches [8, 9, 11].

If we consider now a sample containing more than one paramagnetic species, namely $\mathcal{X} = \{X_1, X_2, \ldots, X_N\}$, and in absence of field gradient applied in the cavity ($\mu = 0$), the measured spectrum $h_\mathcal{X}$ corresponds to the summation of each individual species contribution, that is

$$\forall B \in \mathbb{R}_+, \quad h_\mathcal{X}(B) := \sum_{i=1}^{N} h_{X_i}(B) = \sum_{i=1}^{N} Q_{X_i}\, h_{X_i}^{\mathrm{ref}}(B)\,. \tag{4}$$

In presence of a field gradient ($\mu > 0$), the acquired sinogram $S_\mathcal{X}^\mu$ also follows this summation principle and satisfies, for all $(B, \theta, \varphi) \in \mathbb{R}_+ \times [0, 2\pi] \times [0, \pi]$,

$$S_\mathcal{X}^\mu(B, \theta, \varphi) = \sum_{i=1}^{N} \left(h_{X_i}^\mu * \mathcal{R}_{\theta,\varphi}(U_{X_i})\right)(-B/\mu)\,. \tag{5}$$

The reconstruction of the spatial repartition U_{X_i} of each individual species X_i (for $1 \leq i \leq N$) from the acquired sinogram $S_\mathcal{X}^\mu$ is a source separation problem that we can also address using variational approaches. In the following, we may refer to each X_i as a source instead of a species.

2.2. Discretization

The practical acquisition of EPR measurements is done projection by projection in a discretized manner. Considering a set $\{(\theta_p, \varphi_p)\}_{1 \leq p \leq N_{\mathrm{proj}}}$ made of N_{proj} field gradient orientations, the acquisition of the projection in the direction (θ_p, φ_p) is performed for a finite number (N_B) of homogeneous magnetic field intensities, yielding a sampling grid $(B_n)_{1 \leq n \leq N_B}$. The nodes of this

sampling grid are usually regularly spaced and satisfy

$$\forall n \in \{1, 2, \dots, N_B\}\,, \quad B_n \in B_{\text{CF}} + \left[-\frac{B_{\text{SW}}}{2}, \frac{B_{\text{SW}}}{2}\right]\,, \tag{6}$$

denoting by B_{CF} and B_{SW} the usually called *center field* and *sweep-width* of the homogeneous magnetic field used during the acquisition. From now on, let us denote by $s^{\mu}_{\mathcal{X}}$ the acquired discrete measurements defined by, for all $n \in \{1, 2, \dots, N_B\}$ and for all $p \in \{1, 2, \dots, N_{\text{proj}}\}$,

$$s^{\mu}_{\mathcal{X}}(n, p) = S^{\mu}_{\mathcal{X}}(B_n, \theta_p, \varphi_p)\,. \tag{7}$$

In the following, we may refer to $s^{\mu}_{\mathcal{X}}$ as a *discrete sinogram*. We will also refer to $D_{\text{FOV}} = \frac{B_{\text{SW}}}{\mu}$ as the *field-of-view* of the acquisition.

To complete the discretization process, we need to introduce a discrete representation of the images to be reconstructed. A discretization procedure relying on Shannon sampling Theory was thoroughly described in [11]. Given a source index $i \in \{1, 2, \dots, N\}$ and an image size $M \in \mathbb{N}$, let us consider the discrete image $u_i : \Omega \to \mathbb{R}$ with domain $\Omega = \{0, 1, \dots, M-1\}^3$ obtained by sampling the continuous image U_{X_i} with spatial *sampling step* (or *pixel size*) $\delta = \frac{D_{\text{FOV}}}{M}$ over the field-of-view domain, leading to

$$\forall (k, \ell, m) \in \Omega\,, \quad u_i(k, \ell, m) = U_{X_i}(k\delta, \ell\delta, m\delta)\,. \tag{8}$$

Following the same methodology as in [11], we can link the acquired discrete sinogram $s^{\mu}_{\mathcal{X}}$ to the discrete source images $(u_i)_{1 \le i \le N}$ yielding, for all $(n, p) \in \{1, 2, \dots, N_B\} \times \{1, 2, \dots, N_{\text{proj}}\}$,

$$s^{\mu}_{\mathcal{X}}(n, p) = \sum_{i=1}^{N} A^{\mu}_i u_i(n, p) + \varepsilon(n, p)\,, \tag{9}$$

where each A^{μ}_i is a linear operator such as $A^{\mu}_i u_i$ models the sinogram that would have been acquired if only a single source X_i were present in the cavity. The term $\varepsilon = s^{\mu}_{\mathcal{X}} - \sum_{i=1}^{N} A^{\mu}_i u_i$ formally represents the mismatch between the measured sinogram $s^{\mu}_{\mathcal{X}}$ and the synthetic sinogram $\sum_{i=1}^{N} A^{\mu}_i u_i$ generated from the discretized source images $(u_i)_{1 \le i \le N}$. This term ε aggregates all modeling errors (caused by the approximations that occurred in the various stages of the modeling process, from the physics of the acquisition to the mathematical

discretization of the equations) as well as the instrumental noise corrupting the measurements. In the following, we will neglect the contribution to ε of the modeling errors and assume that ε is fully made of the instrumental noise corrupting the measurement. Besides, we will also assume that $\{\varepsilon(n,p)\}_{n,p}$ is a family of independent and identically distributed centered Gaussian random variables.

3. Inverse problem of source separation

In presence of a single source X, one of the most common method to address EPR image reconstruction from a sinogram acquisition sequentially combines deconvolution and backprojection. Standard deconvolution techniques (such as Wiener filtering) are used to eliminate, inter alia, the contribution of the (dilated) spectrum h_X^μ involved in each projection of the sinogram S_X^μ (see (3)). Then backprojection can be used to compute U_X from the deconvolved sinogram. In the continuous setting, provided an infinite number of measurements and in absence of noise corrupting those measurements, backprojection provides exact reconstruction of U_X. In practice, interpolation techniques and filtering are used to handle discrete measurements and noise. Although this image reconstruction technique remains largely used nowadays [3, 19, 20], variational models have been proven to be more efficient at handling noise, especially when the signal-to-noise ratio is low or when few measurements are available [9, 11, 21, 22]. Besides, conventional filtered backprojection is restricted to single source image reconstruction and is not relevant to address source separation.

In the literature of CW-EPR, the source separation problem is usually addressed using *spectral-spatial* methods [6, 23]. The latter consist in acquiring sinograms for numerous values of field gradient intensities $\{\mu_j\}_{1\leq j\leq N_\mu}$, yielding a large set $\{s_{\mathcal{X}}^{\mu_j}\}_{1\leq j\leq N_\mu}$ of sinogram measurements. Then, the dataset is processed to compute an intermediate four-dimensional image (three spatial dimensions and an additional spectral one) containing an EPR spectrum within each voxel. Source separation can then be addressed voxelwise using monodimensional spectrum-based source separation techniques, as done in [6, 24, 25]. The main drawback of this approach is that it requires a large number of samples along the spectral dimension of the intermediate 4D image, and thus large datasets (with typical values of several hundred for N_μ) and long acquisition times. However, it is worth mentioning that some recent developments in spectral spatial image reconstruction from a limited

number of spectral angles (i.e. reduced values of N_μ), as well as optimization of the projection directions can be helpful to shorten acquisition times (see [26, 27]). Nevertheless, such a voxelwise spectral processing strategy is suboptimal because it does not take into account the spatial coherence of the source images to reconstruct, which is a source of information that can be used to drastically reduce the number of measurements. The variational model that we shall describe below attempts to address the source separation problem globally from drastically less measurements than usual spectral spatial based source separation approaches. This variational model was first proposed in Kerebel's Ph.D. [10] and was experimentally validated in the 2D setting using spectrally well separated species (namely, TAM and TEMPO). In the following, we shall present a more in-depth methodological and experimental study of this source separation technique including its extension to the 3D framework and we shall propose a generalization of the variational model enabling the successful separation of spectrally close species (that are, species with close EPR reference spectra).

3.1. Variational formulation of the source separation problem

To reconstruct the discrete source images $(u_i)_{1\leq i\leq N}$ from a sinogram $s^\mu_{\mathcal{X}}$ we use the regularized least-squares approach proposed in [10]. For a given $\lambda > 0$, we would like to compute

$$\underset{u=(u_1,u_2,\dots,u_N)\in(\mathbb{R}^\Omega)^N}{\operatorname{argmin}} E_\lambda(u) := \frac{1}{2}\left\|\sum_{i=1}^N A^\mu_i u_i - s^\mu_{\mathcal{X}}\right\|_2^2 + \lambda\sum_{i=1}^N \mathrm{TV}(u_i)\,, \tag{10}$$

where $\mathrm{TV}(u_i)$ denotes the total variation of the discrete image u_i. The latter is defined as

$$\mathrm{TV}(u_i) = \sum_{(k,\ell,m)\in\Omega} \|\nabla^{\mathrm{d}} u_i(k,\ell,m)\|_2\,, \tag{11}$$

where ∇^{d} denotes the standard forward finite differences scheme defined by $\nabla^{\mathrm{d}} u_i = (\nabla^{\mathrm{d}}_x u_i, \nabla^{\mathrm{d}}_y u_i, \nabla^{\mathrm{d}}_z u_i)$ and, for all $(k,\ell,m)\in\Omega$,

$$\nabla^{\mathrm{d}}_x u_i(k,\ell,m) = \begin{cases} u_i(k+1,\ell,m) - u_i(k,\ell,m) & \text{if } (k+1,\ell,m)\in\Omega \\ 0 & \text{otherwise,}\end{cases}$$

$$\nabla^{\mathrm{d}}_y u_i(k,\ell,m) = \begin{cases} u_i(k,\ell+1,m) - u_i(k,\ell,m) & \text{if } (k,\ell+1,m)\in\Omega \\ 0 & \text{otherwise,}\end{cases}$$

$$\nabla_z^{\mathrm{d}} u_i(k,\ell,m) = \begin{cases} u_i(k,\ell,m+1) - u_i(k,\ell,m) & \text{if } (k,\ell,m+1) \in \Omega \\ 0 & \text{otherwise.} \end{cases}$$

We can remark that the energy E_λ to minimize in (10) can be decomposed into the sum of two terms using

$$\forall u \in (\mathbb{R}^\Omega)^N\,, \quad E_\lambda(u) = F_\mu(u) + \lambda\, G(u)\,, \tag{12}$$

where $F_\mu(u) = \| \sum_{i=1}^N A_i^\mu u_i - s_{\mathcal{X}}^\mu \|_2^2$ represents a least-squares *data-fidelity* term and $G(u) = \sum_{i=1}^N \mathrm{TV}(u_i)$ is a total variation based *regularity* term. During the minimization of $E_\lambda(u)$ with respect to u, the data-fidelity term $F_\mu(u)$ will enforce the adequacy between the measured sinogram $s_{\mathcal{X}}^\mu$ and the synthetic one generated from the source images $(u_i)_{1\leq i\leq N}$ while the regularity term $G(u)$ will promote the choice of spatially regular source images $(u_i)_{1\leq i\leq N}$. The λ parameter controls the relative weight of the regularity term G with respect to the data-fidelity term F_μ in the energy E_λ to be minimized. In practice, this parameter can be used to control the desired level of spatial regularity in the source images to reconstruct. The reader shall keep in mind that low λ values yield noisy reconstructions while too large λ values yield over-regularized *cartoon looking images*, so that a tradeoff must be found to achieve satisfactory reconstructions (see for instance [11]).

As we shall see in the following, in challenging situations the acquisition of multiple sinograms at different field gradient intensities provides valuable informations to improve the separation. Considering from now on several sinogram acquisitions $\left\{s_{\mathcal{X}}^{\mu_j}\right\}_{1\leq j\leq N_\mu}$ obtained using several values of field gradient intensities $\{\mu_j\}_{1\leq j\leq N_\mu}$, we can generalize the variational problem (10) to globally address the reconstruction of the source images $(u_i)_{1\leq i\leq N}$ from the measured sinograms by computing

$$\underset{u=(u_1,u_2,\ldots,u_N)\in(\mathbb{R}^\Omega)^N}{\operatorname{argmin}} \frac{1}{2}\sum_{j=1}^{N_\mu} \left\| \sum_{i=1}^N A_i^{\mu_j} u_i - s_{\mathcal{X}}^{\mu_j} \right\|_2^2 + \lambda \sum_{i=1}^N \mathrm{TV}(u_i)\,. \tag{13}$$

The variational problem (13) simply amounts to replace the data-fidelity term $F_\mu(u)$ involved in (12) by $F(u) := \sum_{j=1}^{N_\mu} F_{\mu_j}(u)$, that is, the sum of all individual data-fidelity terms F_{μ_j} associated to each acquired sinogram $s_{\mathcal{X}}^{\mu_j}$ (for $1 \leq j \leq N_\mu$). Notice that the field gradient intensity being the only experimental parameter to be changed from one acquisition to another, the level of the noise (that is, the noise standard deviation) corrupting all

sinogram acquisitions should be the same. Therefore, uniform weighting of the individual data-fidelity terms $F_{\mu_j}(u)$ is a relevant way to obtain the global data-fidelity term $F(u)$. For more complicated design of experiments where the sinograms $\{s_{\mathcal{X}}^{\mu_j}\}_{1\leq j\leq N_\mu}$ would be acquired with various settings of acquisition parameters from one acquisition to another (for instance, with different integration time constants), the sinogram acquisitions may exhibit different noise levels and an appropriate weighting of the contribution of each sinogram to the global data-fidelity term would be necessary. We won't consider such kind of experimental design in the following.

3.2. Numerical resolvant scheme

Many efficient optimization algorithms dedicated to convex and nondifferentiable minimization problems like (10) and (13) have been developed during the last two decades (a recent review can be found in [28]). Those algorithms have found many applications in the field of image processing. The algorithms recently proposed in [29–32] are particularly well suited to the source separation problem (13) since the latter efficiently take advantage of the presence of a Lipschitz differentiable (i.e. differentiable with Lipschitz-continuous gradient) term in the energy to minimize. As we shall discuss below, this will be of crucial importance for deriving practically tractable (and computationally efficient) numerical schemes.

Given $u^0 = (u_1^0, u_2^0, \ldots, u_N^0) \in (\mathbb{R}^\Omega)^N$, $p^0 = (p_1^0, p_2^0, \ldots, p_N^0) \in (\mathbb{R}^\Omega \times \mathbb{R}^\Omega \times \mathbb{R}^\Omega)^N$ and two parameters $\tau > 0$ and $\sigma > 0$, the closely related Condat and Vu algorithms [29, 32], that were further generalized in [30], boil down to setting $\overline{u}^{(0)} = u^0$ and to iterating, for $n \geq 0$,

$$\left\{\begin{array}{ll} p^{n+1} = \Pi(p^n + \sigma\lambda K\overline{u}^n) & \text{(14a)} \\ u^{n+1} = u^n - \tau\left(\nabla F(u^n) + \lambda K^* p^{n+1}\right) & \text{(14b)} \\ \overline{u}^{n+1} = 2\,u^{n+1} - u^n & \text{(14c)} \end{array}\right.$$

where $K : u = (u_1, u_2, \ldots, u_N) \mapsto (\nabla^{\mathrm{d}} u_1, \nabla^{\mathrm{d}} u_2, \ldots, \nabla^{\mathrm{d}} u_N)$, K^* denotes the adjoint of K (see Appendix A.1) and where $\Pi : \left(\mathbb{R}^\Omega \times \mathbb{R}^\Omega \times \mathbb{R}^\Omega\right)^N \to \left(\mathbb{R}^\Omega \times \mathbb{R}^\Omega \times \mathbb{R}^\Omega\right)^N$ is defined by, for all $p \in \left(\mathbb{R}^\Omega \times \mathbb{R}^\Omega \times \mathbb{R}^\Omega\right)^N$,

$$\forall (k,\ell,m) \in \Omega\,, \quad \Pi(p)(k,\ell,m) = \left(\frac{p_i(k,\ell,m)}{\max(1, \|p_i(k,\ell,m)\|_2)}\right)_{1\leq i\leq N}.$$

One can easily show that the term $\nabla F(u^n)$ involved in (14b) satisfies

$$\nabla F(u^n) = \left(\sum_{j=1}^{N_\mu} \left(\sum_{i=1}^{N} {A_r^{\mu_j}}^* A_i^{\mu_j} u_i^n \right) - {A_r^{\mu_j}}^* s_{\mathcal{X}}^{\mu_j} \right)_{1 \leq r \leq N} . \tag{15}$$

The quantity $\left(\sum_{j=1}^{N_\mu} {A_r^{\mu_j}}^* s_{\mathcal{X}}^{\mu_j} \right)_{1 \leq r \leq N}$ remains the same along the scheme iterations and can, therefore, be computed once and for all. We refer to [11] (see Algorithm 4 therein) for details about the efficient computation of each term ${A_r^{\mu_j}}^* s_{\mathcal{X}}^{\mu_j}$ (for $1 \leq r \leq N$ and $1 \leq j \leq N_\mu$). As regard the computation of the terms $\left({A_r^{\mu_j}}^* A_i^{\mu_j} u_i^n \right)_{r,i,j}$ involved in (15), it must be noted that, thanks to the underlying Shannon Sampling Theory based discretization schemes of the operators, each ${A_r^{\mu_j}}^* A_i^{\mu_j}$ operator exhibits a Toeplitz circulant structure [10, 11]. Consequently, rather than computing each term ${A_r^{\mu_j}}^* A_i^{\mu_j} u_i^n$ by computing $A_i^{\mu_j} u_i$ then applying ${A_r^{\mu_j}}^*$ to the resulting signal, one can efficiently compute each term ${A_r^{\mu_j}}^* A_i^{\mu_j} u_i^n$ as a whole by means of a circular convolution between the image u_i^n and a three-dimensional kernel $\Psi_{r,i}^{\mu_j}$. Computationally speaking, this operation can be done efficiently through the Fourier domain, using Fast Fourier Transform libraries [33].

More details about the practical computation of the scheme iterations (14a) and (14b), including convergence analysis of the numerical scheme (14) towards a solution of (13) and a pseudocode implementation of the proposed source separation algorithm are provided in Appendix A. One can refer to [29, 32] for an in-depth description of this iterative scheme and its convergence properties. More general insights about the notions of duality and the role of the dual variable p involved in (14a) can be found in [34, 35].

3.3. Two-dimensional imaging and source separation

The acquisition of one or several 3D sinograms using commercial EPR imagers may involve long acquisition times, not to mention the large computational ressources and the long offline computation times needed to achieve the reconstructions, which can be an issue for practical applications. For those reasons, the user may be interested in reducing the number of acquired projections by constraining the magnetic field gradient to lie in a two-dimensional plane (e.g by imposing a fixed value for θ or φ during the acquisition). In such situation, 3D images cannot be efficiently computed due to the too severe lack of measurements. However, one can efficiently perform the reconstruction of the 2D images corresponding to the summation of the

3D images in the direction orthogonal to the magnetic field gradient (more details can be found for instance in [11]). The mathematical operators and reconstruction models described above, as well as the source separation numerical scheme (14), can be easily adapted to this particular setting.

4. Experiments

The following experiments were performed using a Bruker®E540 CW-EPR spectrometer operated in L-band frequencies and controlled using the Xepr© software. The typical working ranges for the acquisition parameters used in our experiments are provided in Table 1. In the case of 3D experiments, we sampled the sphere using independant and uniform sampling of both spherical angles, using N_θ angle nodes in $[0, 2\pi]$ for the polar angle and N_φ nodes in $[0, \pi]$ for the azimuthal angle. This yields $N_{\text{proj}} = N_\theta N_\varphi$ as total number of acquired projection for a given 3D experiment. This acquisition setting corresponds to the standard angular sampling acquisition conditions using Bruker® spectrometers. However other more advanced sampling strategies can be considered, as for instance those proposed in [26, 36]. Indeed, the source separation model proposed in Section 3 does not impose any constraint on the set of projection directions $(\theta_\ell, \varphi_\ell)_{1\leq\ell\leq N_{\text{proj}}}$. Regarding the reconstruction process, a multiscale optimization strategy may be occasionally considered in order to speed up the reconstruction. This means that, a first low-resolution source separation will be performed (for a large value of pixel-size δ). The obtained low-resolution reconstructions will be then upscaled and used as initializers for Scheme (14) to perform source separation at a higher resolution (i.e., for smaller values of pixel-size δ). This numerical trick significantly reduces the computation time required for the reconstruction. We shall explicitly state when such multiscale strategy is being used in the experiments presented below.

In this section, two different kinds of experiments will be carried. In Section 4.1, we will focus on the separation of two species with substantially different EPR spectra, namely a TAM (Tetrathiatriarylmethyl tris-(8-carboxyl-2,2,6,6-tetramethylbenzo-[1,2-d;4,5-d']bis[1,3] dithiol-4-yl)methyl sodium salt, obtained according to [37]) and a TEMPO (4-Hydroxy-2,2,6,6-tetramethylpiperidine-1-oxyl, obtained from sigma Aldrich). Then, in Section 4.2, we will shift our focus towards the more challenging separation of species with closer EPR spectra, a TAM and a DPPH (2,2-diphenyl-1-picrylhydrazyl, Bruker® imaging test sample).

name	description	value or typical range	unit
–	conversion time	20.48	ms
–	time constant	20.48	ms
–	microwave frequency	$1 \sim 1.2$	GHz
–	microwave power	20.05	mW
–	power attenuation	13	dB
–	magnetic field amplitude modulation	0.6	G
–	magnetic field frequency modulation	100	kHz
μ	magnetic field gradient intensity	$5 \sim 40$	G/cm
N_μ	number of acquired sinograms	1 or 2	–
B_{CF}	center-field	400	G
B_{sw}	sweep-width	$52 \sim 208$	G
N_B	number of sample per projection	$500 \sim 2000$	–
N_θ	number of azimuthal angles	50	–
N_φ	number of polar angles	$1 \sim 50$	–
N_{proj}	number of acquired projections per acquired sinogram	$N_\theta N_\varphi$	–
δ	pixel size	$0.1 \sim 1.3$	mm
λ	TV weight in (13)	$10^6 \sim 10^9$	–
n_{iter}	number of iterations for Scheme (14)	$10^4 \sim 10^6$	–

Table 1: **Main acquisition parameters used for data acquisitions. Top** : acquisition parameters. **Bottom** : reconstruction parameters. Precisions about the exact setting of those parameters will be provided for each experiment.

4.1. Separation of spectrally distant species (TAM and TEMPO)

In this section, we focus the separation of TAM and TEMPO. Our experimental sample is made of two test tubes containing 500 µL of either a 2 mmol L^{-1} TAM solution or 5 mmol L^{-1} TEMPO solution. The tubes were placed in the cavity roughly a centimeter apart (see Figure 1). The sample as a whole (i.e., the two tubes) may be refered as a *TAM-TEMPO mixture* in the following, although the two solutions are not mixed together.

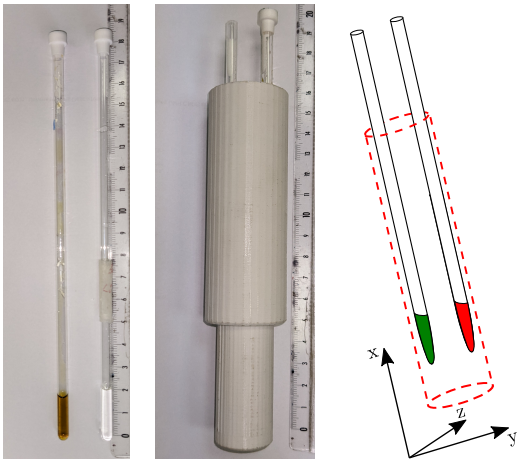

Figure 1: **TAM and TEMPO imaging sample. Left-hand side**: pictures of the imaging sample made of two tubes. One tube is filled with a TAM solution and the second one is filled with a TEMPO solution. The two tubes are maintained together using a plastic holder (see middle picture). **Right-hand side**: schematic representation of the tubes placed in the cavity of the EPR imager. The goal of the source separation problem is to compute the image of each tube separately although the two tubes are placed together in the cavity of the EPR imager during the acquisition.

The acquisition protocol for the TAM and TEMPO compound is straightforward, a single spectrum of the TAM-TEMPO mixture is acquired and then, a single sinogram acquisition is performed (see first row of Figure 2). However, in order to reconstruct a repartition map for each source using the source separation model proposed in Section 3, we need the reference spectrum of each source present in the sample (here TAM and TEMPO). Indeed, the contribution of the reference spectrum h_{X_i} of each source X_i (say for instance here X_1 for the TAM and X_2 for the TEMPO) is mathematically involved in the A_i^μ operators involved in (9), and are thus needed to compute the solution of (13) using Scheme (14). In our experiments, we used the toolbox EasySpin [38] to extract the spectrum of TAM and that of TEMPO from

the acquired spectrum of their mixture (see second row of Figure 2). This toolbox relies on a parameterized model and requires only basic molecular information such as the species's spin system and acquisition parameters.

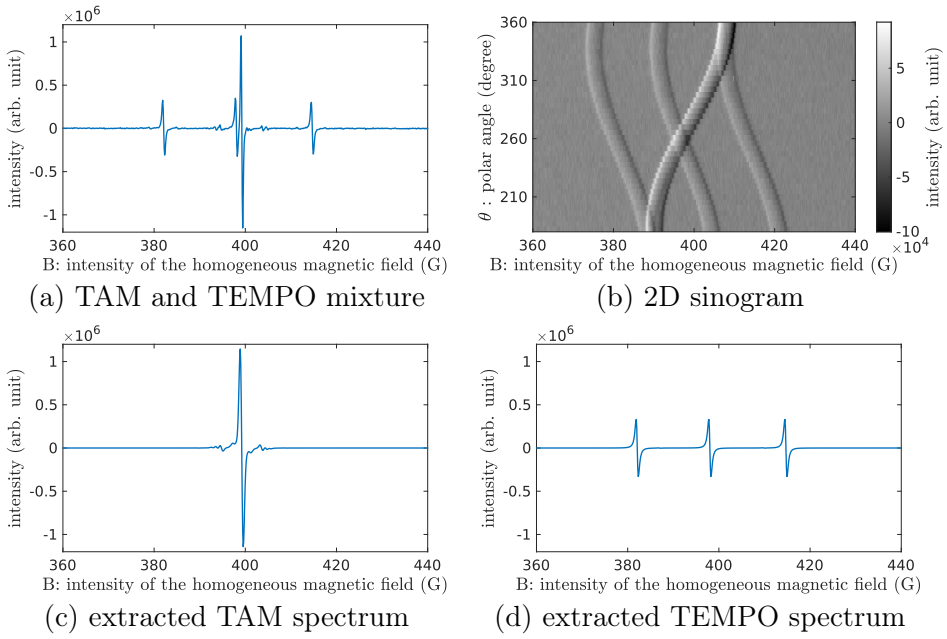

Figure 2: **TAM and TEMPO dataset acquisition and pre-processing (2D experiment).** We display in (a) and (b) the reference spectrum and the sinogram acquisition of the sample containing a tube filled with TAM and a tube filled TEMPO. The setting of the acquisition parameters was $(N_B, B_{\text{sw}}, B_{\text{cf}}, N_\theta, N_\varphi, \mu) = (1200, 130, 400, 50, 1, 10)$ and the acquisition process lasted roughly 20 minutes. We used EasySpin to separate from (a) the reference spectra of the two sources, yielding in (c) the spectrum of TAM and in (d) that of TEMPO (with the relation $(a) \approx (c) + (d)$). Those two separated spectra will be needed to perform the image source separation of both species.

Once the spectra of TAM and TEMPO are extracted from the spectrum of their mixture using EasySpin, they can be used as inputs for our source separation imaging method. An example of 2D image source separation (performed from the dataset in Figure 2 (b)) is presented in Figure 3. Since this experiment was performed in 2D, we only reconstruct here 2D images corresponding to the sum of the 3D volume along the longitudinal direction of the tubes (Z-axis in Figure 1). Therefore, we expect each of the two unmixed sources to be roughly made of a single disk. We can see in Figure 3 that this is indeed what we get using the proposed source separation algorithm.

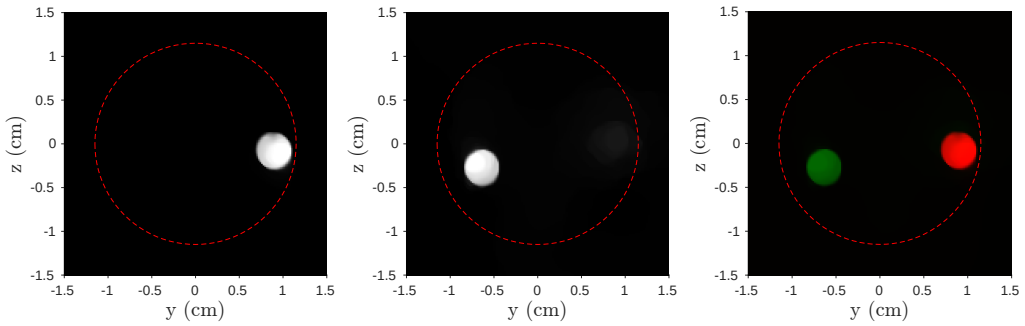

(a) TAM (b) TEMPO (c) TEMPO + TAM

Figure 3: **Separation of TAM and TEMPO filled tubes (2D experiment).** We display in (a) and (b) the two unmixed sources obtained by iterating until convergence the numerical scheme (14). The algorithm parameters used to achieve this reconstruction are $(\lambda, \delta, n_{\text{iter}}) = (10^9, 0.181, 10^5)$. As expected, we can see that in (a) and (b) two disks with disjoint supports representing respectively the 2D repartition maps of the TAM and the TEMPO solutions in the resonance cavity (the latter is indicated using a dashed red line). We display in (c) a merging of those two unmixed sources, where (a) is used as the red channel, (b) is used as the green channel, and the blue channel is set to zero. We can see in this experiment that we could successfully compute the repartition maps of each individual species from a single sinogram acquisition.

When a 3D sinogram acquisition is available, the problem of 3D image source separation can also be addressed using the same algorithm. In this case, the 3D sinogram (see Figure 4 (a)) as well as the extracted spectra of TAM and TEMPO (see Figure 2 (c) and (d)) can be used as inputs of the source separation method to compute two 3D images, each corresponding to the 3D repartition maps of an individual source, as we illustrate in Figure 4 (second row).

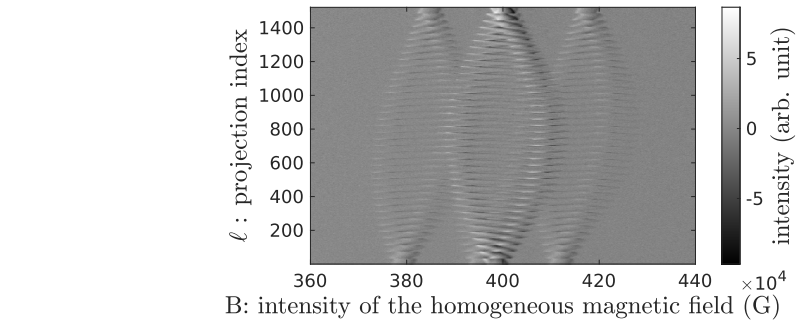

(a) 3D sinogram acquisition of the TAM-TEMPO mixture

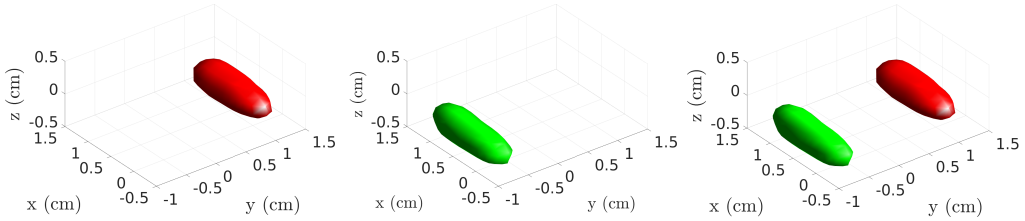

(b) reconstructed TAM source

(c) reconstructed TEMPO source

(d) TEMPO + TAM merging

Figure 4: **Separation of TAM and TEMPO filled tubes (3D experiment).** We display in (a) a 3D sinogram containing 1521 projections acquired using various field gradient directions in the spherical coordinate system (we used $N_\theta = N_\varphi = 39$ angular nodes in both the polar and the azimuthal direction, yielding a total of $N_{\text{proj}} = N_\theta N_\varphi = 1521$ field gradient orientations). The other acquisition parameters $(N_B, B_{\text{sw}}, B_{\text{CF}}, \mu)$ were kept identical to those presented in Figure 2. Using the 3D sinogram (a) and the reference spectra of TAM and TEMPO presented in Figure 2 (c) and (d) as inputs of our image source separation algorithm, we were able to reconstruct the 3D images of the two individual sources. We performed the 3D image source separation using $(\lambda, \delta, n_{\text{iter}}) = (10^8, 1.3, 5 \cdot 10^4)$ as reconstruction parameters. An isosurface of each reconstructed image is displayed in (b) and (c). The reconstructed shapes match well with the shape of a the tubes content. A merging of the two is presented in (d) and enables the visualization of the relative positions of the two tubes in the cavity.

In practice, the different species may not be as clearly separated as the two tubes presented the above experiments. In Figure 5, we addressed the separation of a sample made of a TAM insert immersed into a TEMPO solution. The sample is displayed in Figure 5 (a) and is made of a small eppendorf filled with a 12.5 mM L^{-1} solution of TAM which was placed inside a larger eppendorf filled with a 14 mM L^{-1} solution of TEMPO. A 3D source separation was carried out using our aglorithm, and resulted in a successful separation of the two species, as illustrated in Figure 5. This experiment was

carried out in the 3D mode of the imaging device, therefore we expect to see for the TAM reconstruction a smaller eppendorf-shaped volume contained inside the larger eppendorf-shaped volume representing the TEMPO.

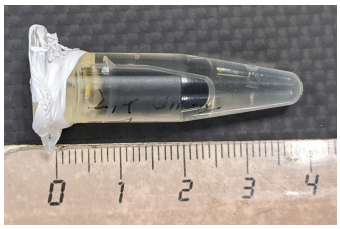

(a) TEMPO solution and inserted TAM

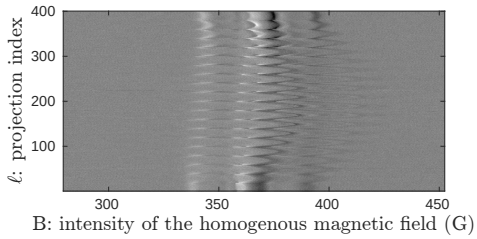

(b) 3D sinogram

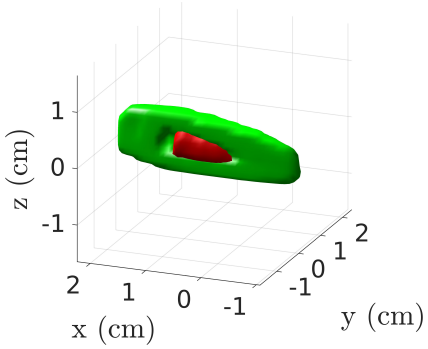

(c) 3D reconstructions of TAM and TEMPO

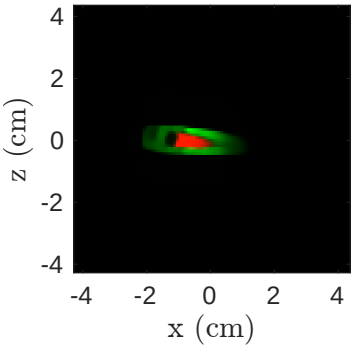

(d) slice of 3D reconstructions

Figure 5: **3D separation of a TAM insert placed into a solution of TEMPO.** We present the experimental setup and the 3D sinogram in panels (a) and (b), respectively. The acquisition parameters for the sinogram depicted in (b) were set as $(N_B, B_{\text{sw}}, B_{\text{CF}}, N_\theta, N_\varphi, \mu) = (1600, 173, 400, 370, 20, 20)$. Utilizing the sinogram from Figure (a) in conjunction with TAM and TEMPO spectra extracted from an acquired mixture spectrum, we performed the reconstruction of two 3D images employing the parameters $(\lambda, \delta, n_{\text{iter}}) = (5 \cdot 10^{-7}, 0.8, 10^4)$. In Figure (c), we present a superposition of two isosurfaces: the TEMPO isosurface is shown in green, with only a half-space displayed, while the complete TAM isosurface is depicted in red. Figure (d) provides a cross-sectional view of Figure (c) at $y = 1$ mm.

In Figure 5 (c), we observe the recovery of an eppendorf of a TAM embedded within an eppendorf of TEMPO in the overlaid images. This distinction becomes even more evident in Figure 5 (d), where there is no detectable signal from TEMPO within the TAM eppendorf, and vice versa. Notably, the black region in Figure 5 (d) corresponds to the lid of the TAM eppendorf.

Those experiments make us confident in the fact that, for spectrally distinct enough species, the source separation can be done efficiently from a

single sinogram acquisition ($N_\mu = 1$), and thus, from drastically less data samples than those needed to achieve spectral-spatial reconstructions.

4.2. Separation of spectrally close species (TAM and DPPH)

In this section, we will consider the problem of separation of two species with close EPR spectra. We consider here TAM and DPPH which both have a single-line EPR spectrum with roughly the same g-factor. The experimental sample is made of an eppendorf filled with a solution of TAM at 17 µmol/L and a Bruker® test sample, made of 8 crystals of DPPH located at the vertices of a cube. A synthetic illustration of the sample is displayed in Figure 6 (a).

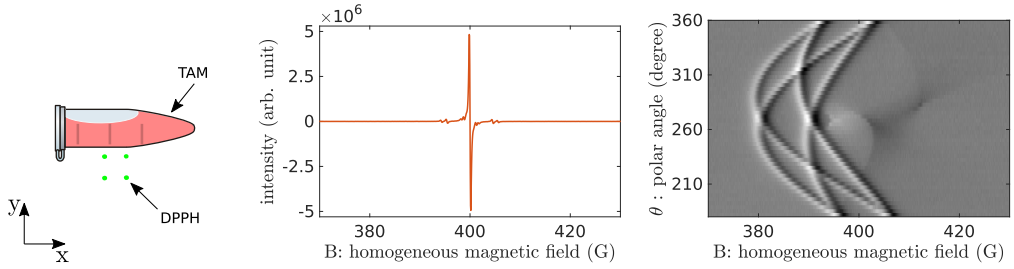

(a) TAM and DPPH sample (top view)

(b) reference spectrum of the TAM-DPPH mixture

(c) 2D sinogram acquisition ($\mu = 20\,\mathrm{G/cm}$)

Figure 6: **TAM and DPPH sample.** We display in (a) a schematic representation of the TAM-DPPH sample which is made of an eppendorf filled with a TAM solution and crystals of DPPH. We display in (b) and (c) a spectrum and a 2D sinogram acquisition of this sample made using $(N_B, B_{\mathrm{sw}}, B_{\mathrm{cf}}, N_\theta, N_\varphi, \mu) = (2000, 104, 400, 50, 1, 20)$. The spectrum displayed in (b) is a mixture of the spectrum of TAM and that of DPPH. Since the EPR spectrum of DPPH has a single line which roughly coincides with the main line of the spectrum of TAM, the contribution of the DPPH crystals to this sample is difficult to detect from (b).

In the following, we will consider EPR datasets acquired from this TAM-DPPH sample and perform the source separation afterward. The acquisition scheme is similar to that presented in the previous section. A single EPR spectrum of the mixture of TAM and DPPH is first acquired (see Figure 6 (b)) and further processed using EasySpin in order to extract from it the reference spectra of each individual species. Then, the acquisition of one (or more) sinogram(s) is performed. We will first consider a dataset containing a single sinogram ($N_\mu = 1$) and then another dataset containing $N_\mu = 2$ sinograms.

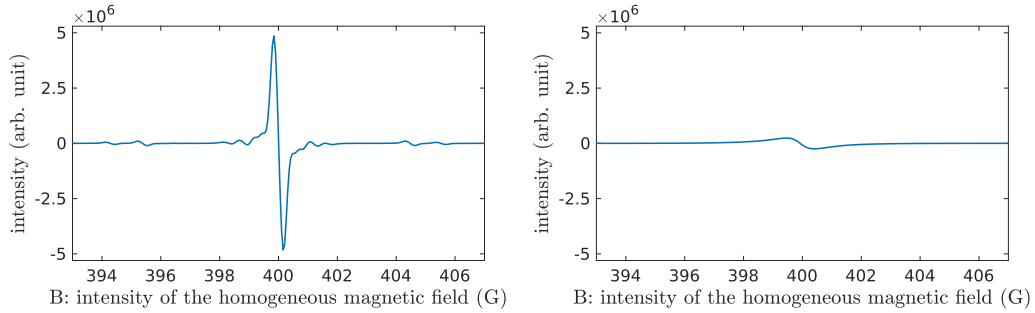

(a) h_{X_1} : extracted TAM spectrum (b) h_{X_2} : extracted DPPH spectrum

Figure 7: **TAM and DPPH spectra separation from the spectrum of their mixture.** We display here the spectrum of TAM (a) and that of DPPH (b) extracted using Easyspin from the spectrum of the TAM-DPPH mixture (Figure 6 (b)). We experimentally validated this separation by comparing the sum $(a) + (b)$ to the spectrum of the TAM-DPPH mixture (comparison not displayed here), yielding a root mean square error of only 0.4% of the peak-to-peak amplitude of the acquired TAM-DPPH mixture spectrum. As we can see, the contribution of the TAM spectrum (a) dominates that of the DPPH crystals (b) in the spectrum of the whole TAM-DPPH mixture.

4.2.1. TAM and DPPH separation from $N_\mu = 1$ sinogram

We first considered a dataset containing the reference spectrum of the TAM and DPPH mixture (see Figure 6 (b)) and a single 2D sinogram acquisition (see Figure 6 (c)). The individual spectra of TAM and DPPH extracted using EasySpin from the spectrum of their mixture are displayed in Figure 7. Those two spectra and the sinogram were used as inputs of our source separation algorithm, yielding the images displayed in Figure 8. As we can see in Figure 8, we were not able to achieve a correct TAM and DPPH image separation from this dataset. We believe that the use of only $N_\mu = 1$ sinogram does not provide sufficient information to separate spectrally close species like TAM and DPPH. Even though we showed that, despite the larger number of unknowns than measurements, the use of the total variation as regularizer of the source separation problem (10) (or (13) with $N_\mu = 1$) enables the accurate separation of spectrally different species such as TAM and TEMPO, the complexity of the problem drastically increases as we consider species with similar spectra, yielding ineffective separation when $N_\mu = 1$.

To address this issue, we suggest to enrich the measured dataset by considering the acquisition of multiple sinograms (i.e., using $N_\mu \geq 2$) with different field gradient intensity values. A mathematical justification of how such multiple sinogram acquisition provides additional information for the

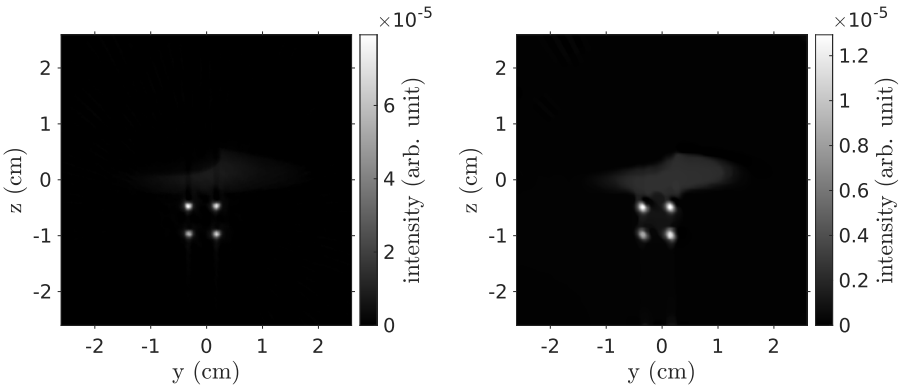

(a) TAM (b) DPPH

Figure 8: **Failed separation of TAM and DPPH from $\mathbf{N_\mu = 1}$ sinogram.** We display the images of TAM (a) and DPPH (b) separated from only $N_\mu = 1$ sinogram acquisition of the mixture (that displayed in Figure 6 (c)) using $(\lambda, n_{\text{iter}}, \delta) = (10^{11}, 10^5, 0.1)$ as set of reconstruction parameters. Due to the nature of the TAM-DPPH sample, the ideal separation would be an image of TAM containing only the TAM solution present in the eppendorf, and an image of DPPH containing only the DPPH crystals. This is clearly not the case here, since we can see shapes coming from the eppendorf and the crystals in both (a) and (b). Besides, we can notice that (a) and (b) have different dynamics (the pixel values of (b) are almost one order of magnitude below those of (a)), so that most of the EPR signal was wrongly reconstructed into the TAM source. The TAM and DPPH species being spectrally close to each other, we believe that their separation is intrinsically more difficult than that of TAM and TEMPO, and that $N_\mu = 1$ sinogram does not provide enough relevant information to perform an accurate separation of those two species.

source separation problem is proposed in Appendix B. Notice that such mutliple sinogram acquisition process is similar to that used for spectral-spatial imaging purpose. However, as mentionned before, the computation of a spectral-spatial image involves the acquisition of a large number of sinograms ($N_\mu \gg 1$) with many different values of field gradient intensities. In our approach, we will consider drastically less measurements and focus on the source separation problem from only $N_\mu = 2$ sinograms. We shall demonstrate now the relevance of this approach over a synthetic dataset first, before illustrating and discussing its efficiency over the real TAM and DPPH source separation experiment.

4.2.2. Separation of synthetic species from $N_\mu = 1$ or $N_\mu = 2$ sinograms

In this section, we consider a synthetic dataset generated from a *sheep-logan* phantom using synthetic spectra of two artificial species X_1 and X_2

with similar shapes as those of TAM and DPPH considered before (see Figure 9). The synthetic sheep-logan phantom was decomposed into the sum of two sub-images (displayed in the last column of Figure 10), each one representing the repartition maps of X_1 and X_2. This synthetic dataset was used to generate two synthetic sinograms of the mixture of $\mathcal{X} = (X_1, X_2)$, acquired using two different field gradient intensities (μ_1 and μ_2 with $\mu_1 < \mu_2$).

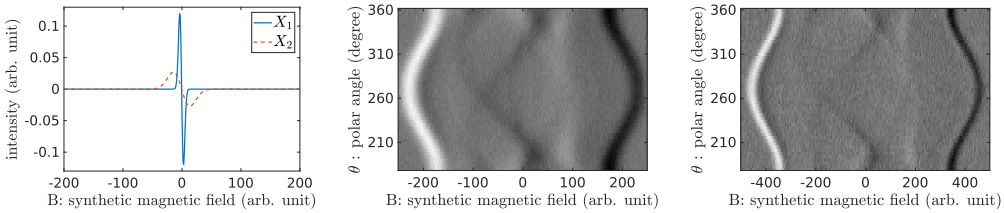

(a) synthetic spectra (b) first sinogram (c) second sinogram

Figure 9: **Synthetic dataset**. We display in (a) the spectra of two synthetic species X_1 and X_2 generated using a Gaussian derivative model of the form $h_{X_i}(B) = -2\,c_i\,B \cdot e^{-c_i B^2}$, using $c_1 = 0.02$, $c_2 = 0.001$. The ratio of the linewidths of those two synthetic spectra is close to 4.5 which is roughly the same linewidths ratio as that of the spectra of TAM and DPPH that we presented in Figure 8. We used two synthetic repartition maps for X_1 and X_2 (displayed in the last column of Figure 10) and generated two synthetic sinograms of the mixture of $\mathcal{X} = (X_1, X_2)$ corresponding to synthetic acquisitions using a low (b) and a large (c) field gradient intensity. Both sinograms were corrupted by a synthetic additive Gaussian noise with same standard deviation. By construction, we obtain in (b) a synthetic sinogram blurrier but with better SNR than that displayed in (c), which is consistent with real-life acquisition.

We used our source separation algorithm to separate the two synthetical species using either $N_\mu = 1$ sinogram (see the first row of Figure 10 for the resulting separation) or $N_\mu = 2$ sinograms (see the second row of Figure 10). Similarly to what we already observed on our real experiment using TAM and DPPH, our algorithm fails to perform the separation of the two species from $N_\mu = 1$ sinogram. However, the use of $N_\mu = 2$ sinograms yields to a satisfactory separation. The reconstructions displayed in Figure 10 were obtained using a mutliscaled strategy in order to speed-up the computation. A first separation was done at a coarse scale using $(\lambda, n_{iter}) = (500, 10^5)$. This coarse scaled image separation was obtained in about 1 minute using a standard laptop. Then, we performed a scale refinement process : the coarse images were upscaled by a factor two (using bilinear interpolation) and used as initializers of scheme (14) to perform image separation at a (twice) thiner scale. This second pass was done using $(\lambda, n_{iter}) = (250, 10^5)$. A final third

pass was done using $(\lambda, n_{iter}) = (50, 3.5 \cdot 10^3)$. The whole image separation process eventually ended in around 10 minutes.

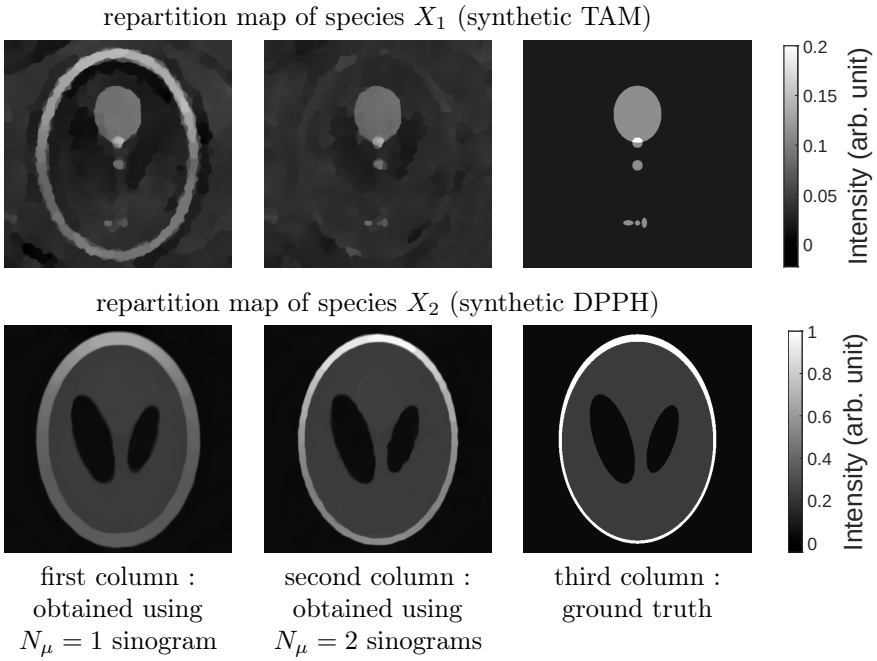

Figure 10: **Source separation using one or two sinograms**. The repartition maps of the two artificial species X_1 and X_2 that we considered in our synthetic experiment are made of ellipses (extracted from a sheep-logan phantom). They are represented in the third column of this figure (top : X_1, bottom : X_2) and correspond to the ideal source images that we would like to reconstruct from the synthetical dataset presented in Figure 9. We display in the left column the two source images reconstructed using only $N_\mu = 1$ sinogram (that displayed in Figure 9 (b)), and we display in the middle column that reconstructed using $N_\mu = 2$ sinograms. We can see in the first column that the reconstruction of source X_1 is substantially different from the ground truth, especially due to the presence in the reconstructed image of a large (outer) ellipse that belongs in fact to source X_2. This artifact in the reconstruction is drastically diminished when looking at the middle column, where both reconstructed source images X_1 and X_2 better match the ground truth images. This experiment illustrates how the addition of another sinogram to the dataset may substencially improve the quality of the source separation of spectrally close species.

4.2.3. TAM and DPPH separation from $N_\mu = 2$ sinograms

From now, let us focus back on the TAM-DPPH real experiment and try to achieve a better image separation than that obtained in Section 4.2.1 by considering a dataset containing $N_\mu = 2$ (instead of $N_\mu = 1$) sinograms.

The acquisition of such a dataset involves slight changes in the whole acquisition protocol that we designed as follows. The acquisition of the two sinograms $(s_{\mathcal{X}}^{\mu_1}, s_{\mathcal{X}}^{\mu_2})$ using two different field gradient intensities (μ_1 and μ_2, with $\mu_1 < \mu_2$) is made sequentially. To ease the data acquisition and the image reconstruction processes, we decided to keep constant the number of acquired samples per projection (N_B), the center-field (B_{CF}), the conversion time, the time constant, as well as the field-of-view diameter during both sinogram acquisitions. This means that if a given sweep-width $B_{\text{SW}}^{(1)}$ is used for the acquisition of the first sinogram $s_{\mathcal{X}}^{\mu_1}$, we need to perform the acquisition of the second sinogram $s_{\mathcal{X}}^{\mu_2}$ using a sweep-width of

$$B_{\text{SW}}^{(2)} = \frac{\mu_2}{\mu_1} B_{\text{SW}}^{(1)} .$$

Notice that sinogram $s_{\mathcal{X}}^{\mu_2}$ will exhibit a lower signal-to-noise ratio than sinogram $s_{\mathcal{X}}^{\mu_1}$ (because $\mu_2 > \mu_1$). This however is taken into account in the model in (13) where each data fidelity term F_{μ_j} are weighted equally. In our experiments, along the acquisition of each sinogram $s_{\mathcal{X}}^{\mu_j}$ $(1 \leq j \leq 2)$, we performed the acquisition of a spectrum $h_{\mathcal{X}}^{(j)}$ of the TAM-DPPH mixture using the same sampling grid as that used for the acquisition of $s_{\mathcal{X}}^{\mu_j}$ (i.e., using $B_{\text{SW}}^{(j)}$ as sweep-width). Therefore, at the end of the acquisition process, we end up with a set of two reference spectra of the TAM-DPPH mixture $(h_{\mathcal{X}}^{(1)}, h_{\mathcal{X}}^{(2)})$ and a set of two associated sinograms $(s_{\mathcal{X}}^{\mu_1}, s_{\mathcal{X}}^{\mu_2})$, as displayed in Figure 11.

Before using our algorithm to perform the image source separation, we need to compute for each acquired sinogram, the reference spectra of the different species (here TAM and DPPH) sampled over the same sampling grid as the sinogram. Theoretically, one could use only one reference spectrum acquisition of the TAM-DPPH mixture, let us say for instance $h_{\mathcal{X}}^{(1)}$, perform the extraction of TAM and DPPH spectra from this acquisition, and use Easyspin to generate the spectra of the two species using either $B_{\text{SW}}^{(1)}$ of $B_{\text{SW}}^{(2)}$ as sweep-width. Although we did considered this approach, we found that, using our Bruker® spectrometer, the single change of the sweep-width from one acquisition to another yielded slightly modified spectral shapes (we observed slight line shifts and amplitude changes in the acquired spectra, as illustrated in Figure 12), making the spectra extracted from $h_{\mathcal{X}}^{(1)}$ somehow inconsistent with those actually involved in the second sinogram $s_{\mathcal{X}}^{\mu_2}$).

Unfortunately, this can negatively impact the image separation. In order to address this issue, we used EasySpin to extract at once from the whole

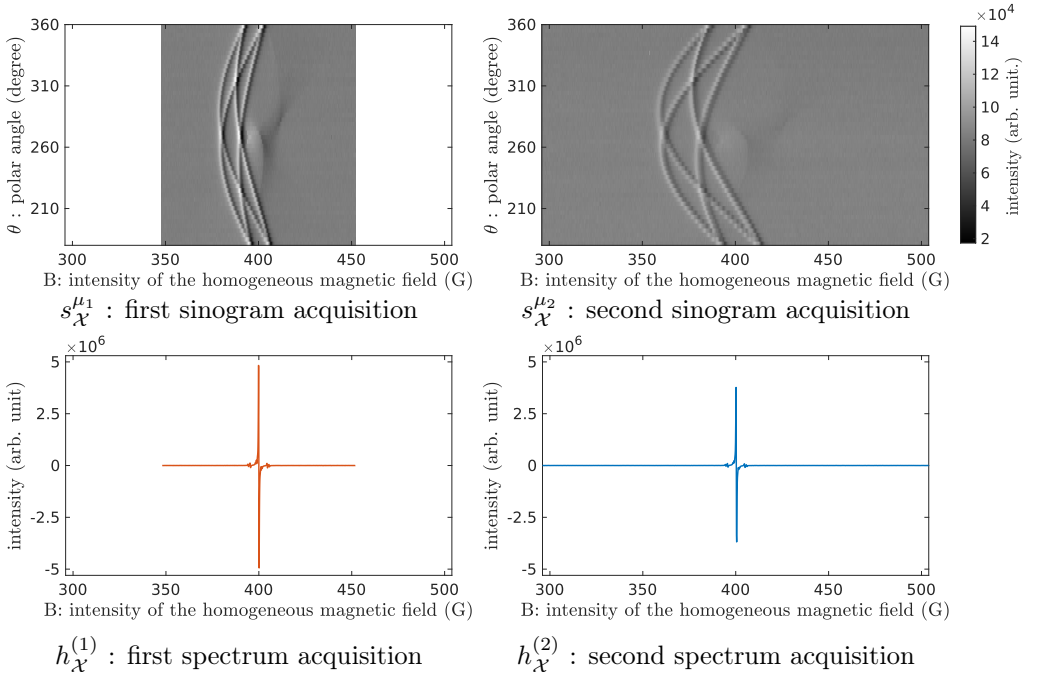

Figure 11: **Acquisition of a dataset made of $N_\mu = 2$ sinograms and two associated reference spectra of the TAM-DPPH mixture.** In the first column, we display (top) the sinogram acquired using a low field gradient intensity ($\mu_1 = 20\,\mathrm{G/cm}$, $B_{\mathrm{sw}} = 104\,\mathrm{G}$) and (bottom) the associated spectrum acqusition $h_{\mathcal{X}}^{(1)}$ of the TAM-DPPH mixture. In the second column, we display (top) a sinogram acquired using a higher field gradient intensity ($\mu_2 = 40\,\mathrm{G/cm}$, $B_{\mathrm{sw}} = 208\,\mathrm{G}$) and (bottom) the associated spectrum acquisition $h_{\mathcal{X}}^{(2)}$ of the TAM-DPPH mixture. The other acquisition parameters were set to $(N_B, B_{\mathrm{CF}}, N_\theta) = (2000, 400, 50)$ for this experiment. Although the spectra $h_{\mathcal{X}}^{(1)}$ and $h_{\mathcal{X}}^{(2)}$ should theoretically coincide over their common sampling range, we observe in practice slight differences between those two signals (a close-up view of their central line is displayed in Figure 12).

set $(h_{\mathcal{X}}^{(1)}, h_{\mathcal{X}}^{(2)})$ the reference spectra of the TAM and DPPH over the same sampling grid as $s_{\mathcal{X}}^{\mu_1}$ and $s_{\mathcal{X}}^{\mu_2}$, taking into account potential shifts and amplitude changes between the two acquisitions. At the end of this process, we end up with the set of reference spectra $\left(h_{X_i}^{(j)}\right)$ (for $1 \leq i \leq 2$ and $1 \leq j \leq 2$) needed in our source separation model. The result of this spectrum separation process is displayed in Appendix C. Finally, the source separation result obtained by processing the two sinograms displayed in Figure 11 using our source separation algorithm are presented in Figure 13. We again used a

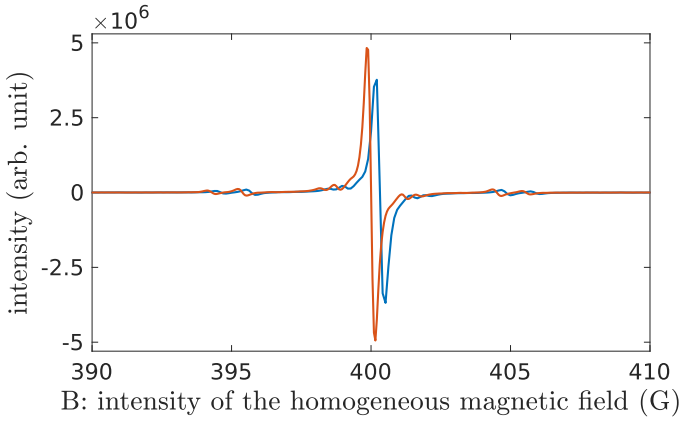

Figure 12: **Close-up view of the two acquired spectra presented in Figure 11.** We display here a close-up view of the spectra $h_{\mathcal{X}}^{(1)}$ and $h_{\mathcal{X}}^{(2)}$ displayed in Figure 11. As we can see, both signals are slightly shifted and exhibit different amplitudes. For that reason, the TAM and DPPH spectra extracted using EasySpin from $h_{\mathcal{X}}^{(1)}$ are in practice inconsistent with those involved into $h_{\mathcal{X}}^{(2)}$ as well as those involved in modeling of the sinogram $s_{\mathcal{X}}^{\mu_2}$. We found that TAM and DPPH spectra separation should be addressed from the whole set $(h_{\mathcal{X}}^{(1)}, h_{\mathcal{X}}^{(2)})$ in order to avoid the apprearance of important artifacts during the image separation process.

multiscale strategy in order to speed up the image source separation process starting with a preliminary separation using $(\lambda, n_{iter}, \delta) = (4 \cdot 10^{12}, 10^5, 0.52)$ followed by a second one using $(\lambda, n_{iter}, \delta) = (2 \cdot 10^{12}, 10^7, 0.26)$ and finally a last pass using $(\lambda, n_{iter}, \delta) = (10^{12}, 10^7, 0.13)$. The whole source image separation process ended in roughly 10 minutes. We can see in Figure 13 that the image separation process is drastically improved when we consider a dataset containing $N_\mu = 2$ sinograms instead of $N_\mu = 1$. The separation remains perfectible, especially because small errors in the separation of the TAM and DPPH spectra from the spectrum of their mixture can cause artifacts in the overall image separation.

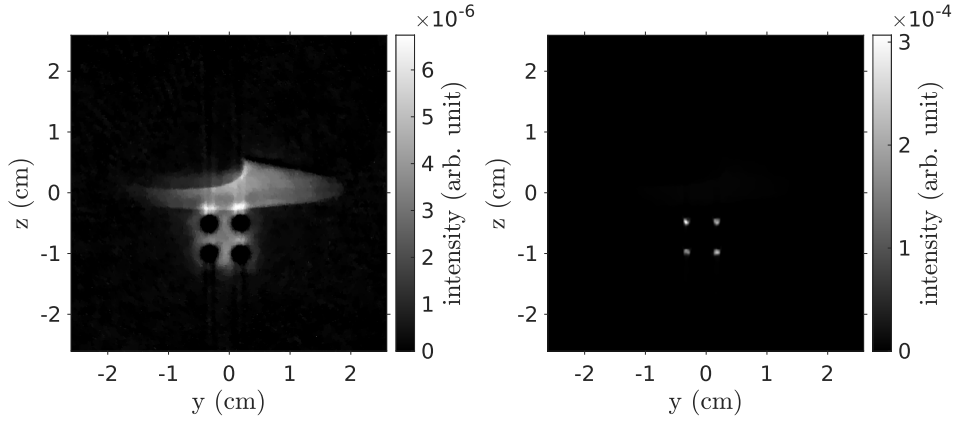

(a) TAM (b) DPPH

Figure 13: **Separation of TAM and DPPH from $\mathbf{N_\mu = 2}$ sinograms.** We display the image of TAM (a) and DPPH (b) separated from the two sinograms presented in Figure 11. We can clearly see in (a) the TAM solution placed in the eppendorf and we can see in (b) the DPPH crystals of the Bruker® sample cube. The separation is effective in the sense that we find no signal coming from the DPPH in (a) and no signal coming from the TAM in (b). However, we can observe in (a) some spurious signal around the location of the DPPH crystals. We believe that this kind of artifact is a consequence of imperfections coming from the separation of the TAM and DPPH spectra from the spectrum of their mixture. However, this experiments still confirms that, as we observed using synthetic dataset, the image separation can be dramatically improved by considering a dataset made of $N_\mu = 2$ (instead of $N_\mu = 1$) sinograms.

5. Conclusion and perspectives

The state-of-the-art approach to tackle the problem of source separation is spectral-spatial imaging, which involves acquiring a set of sinograms at different gradient intensities, followed by a voxel-wise separation. However, this method often requires a lengthy acquisition time due to the sinogram collection time. To address this limitation, this work proposes a procedure that aims to reduce the required data volume by employing a variational formulation of the source separation problem. We've shown that for two paragmanetic species, or sources, with moderately different spectra, here a TAM and a TEMPO compound, our method yields separate 2D and 3D repartition maps for both compound using one sinogram acquisition. However difficulties arise for two sources with similar spectra, such as a TAM and a DPPH compound, when using only one sinogram. With the addition of a second sinogram obtained at a different gradient intensity μ the TAM-

DPPH separation was successfully performed, yielding a clearer separation, as illustrated in Figure 13. We have demonstrated that, for the separation of two sources, a maximum of $N_\mu \leq 2$ is required, whether the sources have different or similar spectra. This process can be compared to spectral-spatial acquisition, albeit requiring only a few additional sinograms, at most equal to the number of sources.

The initial step in the separation method involves extracting the spectra from the acquired mixture, relying on prior knowledge of the compounds present, here this step is done with the easyspin toolbox. Mistakes in fitting, such as when fitting sources that shares the same number of lines, g-factor, and linewidth, can lead to artifacts during the separation process as observed in Figure 13. To enhance the accuracy of the fitting step, future research should consider a better model to incorporate the acquisition filter of the spectrometer into the methodology. Nevertheless, in the case of using a spectral-spatial imaging modality, the spectra separation step would need to be performed for each voxel of the reconstructed image, which would be more challenging. To address this issue, a possible solution would be to incorporate the spectra extraction step within the variational formulation of the model for example using a blind source separation method. This should enable a more streamlined and efficient separation process, such an approach warrants further investigation and development in future studies.

The method proposed relies on a single parameter λ which depends on both the noise level of the acquisition and the characteristics of the object being imaged. This parameters needs to be fine-tuned, however when the user doesn't need to recover fine details the tuning is simplified. Indeed in such case, setting λ too high is generally less detrimental than setting it too low, reducing the need for extensive trial and error. To enhance the model further, an adjustment could be made to consider the differences in shapes of the objects being imaged. Specifically, during the optimization step, the same parameter λ is currently applied to all source images $(u_i)_{1\leq i\leq N}$. However, if one of the sources represents a larger object, all else being equal its total variation tends to be higher compared to a smaller object. Consequently, this can lead to a discrepancy in the reconstruction, favoring smaller objects more during the optimization process. To address this issue, we can introduce a regularization parameter (TV Weight) λ_i for each source u_i. It is relatively straightforward to mathematically incorporate this condition into the model.

This work can be useful in every cases where a spectral-spatial acquisition is required such as multimodal image registration with different probes

or radical characterisation [6]. When directly comparing this work and a classical spectral-spatial acquisition in such use cases the acquisition time can be shortened by several orders of magnitude.

While our study primarily emphasized separating two sources, it's important to highlight that there is no inherent restriction on the number of sources that can be separated. By accurately modeling spectra and potentially obtaining multiple sinograms while still having $N_\mu \leq N$, the separation method can be extended to encompass more than two sources, even when their spectra share similarities.

Spectral spatial imaging finds its most notable application in oximetry. In the case of using a TAM compound whose linewidth expands in the presence of oxygen, one can perceive this as a source separation problem with an infinite number of sources. Nevertheless, we can consider a TAM with a linewidth dilation caused by oxygen concentration c_1 as a separate source from another TAM with a linewidth dilation caused by oxygen concentration c_2, enabling us to achieve source separation between these two sources.

The proposed method holds significant potential for direct application. For instance, it could be effectively employed in pH measurement, exemplified by the utilization of the HOPE probe [39]. In this context, the probe exists in both a base and an acid form, each exhibiting a distinct spectra. The resulting mixture is essentially the combination of these two forms. Moreover, the method can be readily applied to plant cell imaging, leveraging cPTIO [40] as a valuable tool in this regard.

We believe that the framework presented here can be applied to open new perspectives for EPR imaging in science thanks to the speeding up of the data collection, the simplifying of the post treatement of the separation and the potential to be used with compounds exhibiting similar spectra.

Appendix A. Numerical details about the proposed source separation algorithm

Appendix A.1. Computation of K^*

First, let us recall that, for any $u = (u_1, u_2, \ldots, u_N)$, the signal Ku corresponds to the stacking of the $\nabla^{\mathrm{d}} u_i$ (for $1 \leq i \leq N$), that is,

$$Ku = (\nabla^{\mathrm{d}} u_1, \nabla^{\mathrm{d}} u_2, \ldots, \nabla^{\mathrm{d}} u_N)\,. \tag{A.1}$$

Consequently, for any $p = (p_1, p_2, \ldots, p_N) \in (\mathbb{R}^\Omega \times \mathbb{R}^\Omega \times \mathbb{R}^\Omega)^N$, K^*p is the stacking of the $\nabla^{\mathrm{d}^*} p_i$ (for $1 \leq i \leq N$), denoting by ∇^{d^*} the adjoint

of the discrete forward differences scheme ∇^{d}. Besides, using the notation $p_i = (p_i^x, p_i^y, p_i^z)$ for all $i \in \{1, 2, \dots, N\}$, we can easily compute $\nabla^* p_i$ using

$$\nabla^{\mathrm{d}^*} p_i = \nabla_x^{\mathrm{d}^*} p_i^x + \nabla_y^{\mathrm{d}^*} p_i^y + \nabla_z^{\mathrm{d}^*} p_i^z \,, \tag{A.2}$$

and, for all $(k, \ell, m) \in \Omega$,

$$\nabla_x^{\mathrm{d}^*} p_i^x(k,\ell,m) = \begin{cases} -p_i^x(1,\ell,m) & \text{if } k = 1 \\ -p_i^x(k,\ell,m) + p_i^x(k-1,\ell,m) & \text{if } 2 \leq k \leq M-1 \\ p_i^x(M-1,\ell,m) & \text{if } k = M \end{cases},$$

$$\nabla_y^{\mathrm{d}^*} p_i^y(k,\ell,m) = \begin{cases} -p_i^y(k,1,m) & \text{if } \ell = 1 \\ -p_i^y(k,\ell,m) + p_i^y(k,\ell-1,m) & \text{if } 2 \leq \ell \leq M-1 \\ p_i^y(k,M-1,m) & \text{if } \ell = M \end{cases},$$

$$\nabla_z^{\mathrm{d}^*} p_i^z(k,\ell,m) = \begin{cases} -p_i^z(k,\ell,1) & \text{if } m = 1 \\ -p_i^z(k,\ell,m) + p_i^z(k,\ell,m-1) & \text{if } 2 \leq m \leq M-1 \\ p_i^z(k,\ell,M-1) & \text{if } m = M \end{cases}.$$

Therefore, for any $p = (p_1, p_2, \dots, p_N) \in (\mathbb{R}^\Omega \times \mathbb{R}^\Omega \times R^\Omega)^N$, one can easily compute

$$K^* p = (\nabla^{\mathrm{d}^*} p_1, \nabla^{\mathrm{d}^*} p_2, \dots, \nabla^{\mathrm{d}^*} p_N) \,. \tag{A.3}$$

Appendix A.2. Computation of (14b)

As mentioned in Section 3.2, each term $\left(A_r^{\mu_j *} A_i^{\mu_j} u_i^n\right)_{r,i,j}$ involved in (15) can be evaluated by means of a circular convolution between a (fixed) three-dimensional kernel $\Psi_{r,i}^{\mu_j}$ and the latent source image u_i^n. This is computationally rather efficient than computing sequentially $v_{i,j}^n := A_i^{\mu_j} u_i^n$ and $A_r^{\mu_j *} v_{i,j}^n$ afterwards. The main reason is that the circular convolution between the kernel $\Psi_{r,i}^{\mu_j}$ and the source image u_i^n can be computed efficiently using Fast Fourier Transform algorithms, while the systematic numerical evalutation of $A_i^{\mu_j} u_i^n$ and that of $A_r^{\mu_j *} v_{i,j}^n$ at each iteration n of the numerical scheme (14) would involve substentially higher intensive computations (based on Nonequispaced Discrete Fourier Transforms or interpolations schemes in the 3D space, depending on the discretization scheme used for the Radon operator). For the sake of completeness, we provide below more details about the practical evaluation the kernels $\Psi_{i,j}^{\mu_j}$ and that of those terms $\left(A_r^{\mu_j *} A_i^{\mu_j} u_i^n\right)_{r,i,j}$. All

formula provided below can be obtained following the same methodology as in the proof of [11, Proposition 1].

Given a monodimensional signal $h : \{0, 1, \ldots, n-1\} \to \mathbb{R}$, we denote by $\mathrm{DFT}(h)$ the discrete Fourier transform of h, that is, the complex-valued n-periodical signal defined by

$$\forall \alpha \in \mathbb{Z}\,, \quad \mathrm{DFT}(h)(\alpha) = \sum_{k=0}^{n-1} h(k)\, e^{-\frac{2\imath\pi\alpha k}{n}}\,,$$

denoting by $\imath$ the imaginary unit (i.e., $\imath^2 = -1$), and we denote by IDFT the inverse of the DFT operator. We shall also consider below the standard extension of the DFT and IDFT operators to multidimensional signals.

Let us denote by $h^d_{i,j}$ the discrete signal obtained by sampling the reference spectrum h_{X_i} over the same homogeneous magnetic field sampling grid as the acquired sinogram $s^{\mu_j}_{\mathcal{X}}$. Now, let us set $\Upsilon = \{0, 1, \ldots, 2M-1\}^3$ and define $\Psi^{\mu_j}_{r,i} : \Upsilon \to \mathbb{R}$ by, for all $x \in \Upsilon$,

$$\Psi^{\mu_j}_{r,i}(x) = \frac{\delta^6}{N_B} \sum_{\substack{-\frac{M}{2} \leq \alpha < \frac{M}{2} \\ 1 \leq \ell \leq N_{\mathrm{proj}}}} \overline{\mathrm{DFT}(h^d_{r,j})(\alpha)} \mathrm{DFT}(h^d_{i,j})(\alpha)\, e^{2\imath\pi \frac{\alpha}{M} \langle x\,, e_{(\theta_\ell, \varphi_\ell)} \rangle}\,, \tag{A.4}$$

denoting by $\overline{z}$ the complex conjugate of $z \in \mathbb{C}$. Then, one can show that, for all $(i, r) \in \{1, 2, \ldots, N\}^2$ and for all $j \in \{1, 2, \ldots, N_\mu\}$, we have

$$\forall (k, \ell, m) \in \Omega\,, \quad A^{\mu_j *}_r A^{\mu_j}_i u^n_i\,(k, \ell, m) = \left(\Psi^{\mu_j}_{r,i} \circledast Z u^n_i\right)(k, \ell, m), \tag{A.5}$$

where $Z u^n_i : \Upsilon \to \mathbb{R}$ is the zero-padding extension of u^n_i over Υ, defined by

$$\forall (k, \ell, m) \in \Upsilon\,, \quad Z u^n_i(k, \ell, m) = \begin{cases} u^n_i(k, \ell, m) & \text{if } (k, \ell, m) \in \Omega \\ 0 & \text{otherwise,} \end{cases} \tag{A.6}$$

and where $\circledast$ denotes the circular convolution operator which is defined in the Fourier domain by

$$\forall (u, v) \in \mathbb{R}^\Upsilon \times \mathbb{R}^\Upsilon\,,\ \forall \alpha \in \Upsilon\,, \quad \mathrm{DFT}(u \circledast v)(\alpha) = \mathrm{DFT}(u)(\alpha) \cdot \mathrm{DFT}(v)(\alpha)\,.$$

Notice that (A.5) means that the signal $A^{\mu_j *}_r A^{\mu_j}_i u^n_i$ (that lies in $\mathbb{R}^\Omega$) corresponds to the restriction to Ω of the signal $\Psi^{\mu_j}_{r,i} \circledast Z u^n_i$ (that lies in $\mathbb{R}^\Upsilon$). More precisely, denoting by $R_\Omega : \mathbb{R}^\Upsilon \to \mathbb{R}^\Omega$ the operator of restriction to Ω (i.e.,

for all $v \in \mathbb{R}^{\Upsilon}$, $R_\Omega v$ denotes the restriction of the signal v to the domain $\Omega \subset \Upsilon$), we have

$$A_r^{\mu_j *} A_i^{\mu_j} u_i^n = R_\Omega \left(\Psi_{r,i}^{\mu_j} \circledast Z u_i^n \right) .$$

Consequently, by setting $\Psi_{r,i} := \sum_{j=1}^{N_\mu} \Psi_{r,i}^{\mu_j}$ and interchanging the sums in (15), we get

$$\begin{aligned} \nabla F(u^n) &= \left(\sum_{i=1}^{N} \sum_{j=1}^{N_\mu} R_\Omega \left(\Psi_{r,i}^{\mu_j} \circledast Z u_i^n \right) - \sum_{j=1}^{N_\mu} A_r^{\mu_j *} s_{\mathcal{X}}^{\mu_j} \right)_{1 \le r \le N} \\ &= \left(\sum_{i=1}^{N} R_\Omega \left(\Psi_{r,i} \circledast Z u_i^n \right) - \sum_{j=1}^{N_\mu} A_r^{\mu_j *} s_{\mathcal{X}}^{\mu_j} \right)_{1 \le r \le N} . \end{aligned} \tag{A.7}$$

The computation of the $\Psi_{r,i}$ kernels (for $(r,i) \in \{1,2,\dots,N\}^2$) as well as that of the term $\sum_{j=1}^{N_\mu} A_r^{\mu_j *} s_{\mathcal{X}}^{\mu_j}$ (for $1 \le r \le N$) can be done once and for all since those terms remain unchanged during all the scheme iterations in (14). The precomputation of those terms can be efficiently done using Nonequispaced Discrete Fourier Transforms libraries, such as [41], before starting the iterations of Scheme (14).

Appendix A.3. Convergence of (14)

The convergence of (14) towards a solution of (13) is ensured by [30, Theorem 1] as long as the parameters τ and σ fulfill the condition

$$\left(\frac{1}{\tau} - L_F \right) \frac{1}{\sigma} \ge \lambda^2 |||K|||^2 , \tag{A.8}$$

where L_F denotes a Lipschitz constant of ∇F and $|||K|||$ denotes the ℓ^2-induced norm of the operator K. First, let us focus on the computation of a Lipschitz constant of ∇F. Let $u \in (\mathbb{R}^\Omega)^N$ and $v \in (\mathbb{R}^\Omega)^N$, using (A.7), we get

$$\begin{aligned} \|\nabla F(u) - \nabla F(v)\|_2^2 &= \sum_{r=1}^{N} \left\| \sum_{i=1}^{N} R_\Omega \left(\Psi_{r,i} \circledast (Z u_i - Z v_i) \right) \right\|_2^2 \\ &\le \sum_{r=1}^{N} \sum_{i=1}^{N} \| \Psi_{r,i} \circledast (Z u_i - Z v_i) \|_2^2 \end{aligned}$$

by triangle inequality and using $|||R_\Omega||| = 1$. Therefore, using Parseval identity, we get

$$\begin{aligned}\|\nabla F(u) - \nabla F(v)\|_2^2 &\leq \frac{1}{M^3}\sum_{r=1}^{N}\sum_{i=1}^{N}\|\mathrm{DFT}(\Psi_{r,i})\cdot\mathrm{DFT}(Zu_i - Zv_i)\|_2^2 \\ &\leq \frac{1}{M^3}\sum_{r=1}^{N}\sum_{i=1}^{N}\|\mathrm{DFT}(\Psi_{r,i})\|_\infty^2\cdot\|\mathrm{DFT}(Zu_i - Zv_i)\|_2^2\end{aligned}$$

Thus, by setting

$$L_F = \sqrt{\max_{1\leq i\leq N}\sum_{r=1}^{N}\|\mathrm{DFT}(\Psi_{r,i})\|_\infty^2} \tag{A.9}$$

we get

$$\|\nabla F(u) - \nabla F(v)\|_2^2 \leq \frac{L_F^2}{M^3}\sum_{i=1}^{N}\|\mathrm{DFT}(Zu_i - Zv_i)\|_2^2 = L_F^2\|Zu - Zv\|_2^2\,,$$

and since $\|Zu - Zv\|_2 = \|u - v\|_2$, we end up with

$$\|\nabla F(u) - \nabla F(v)\|_2 \leq L_F\|u - v\|_2$$

showing that ∇F is L_F-Lipschitz. Now that the Lipschitz constant of ∇F is computed, let us focus on the term $|||K|||$ involved in (A.8). Since we can easily show that $|||\nabla||| \leq \sqrt{12}$, it follows that

$$\forall u \in (\mathbb{R}^\Omega)^N\,,\quad \|Ku\|_2^2 = \sum_{i=1}^{N}\|\nabla u_i\|_2^2 \leq 12\sum_{i=1}^{N}\|u_i\|_2^2 = 12\|u\|_2^2\,,$$

showing that $|||K||| \leq \sqrt{12}$. Finally, by setting

$$\tau = \frac{1}{2L_F}\quad\text{and}\quad\sigma = \frac{L_F}{12\lambda^2}\,,$$

we ensure that (A.8) is fulfilled, and that scheme (14) converges towards a solution of (13).

Appendix A.4. Pseudocode implementation of the proposed source separation algorithm

In this section, a pseudocode implementation of the source separation algorithm is provided. This pseudocode was split into two modules. Algorithm 1 is dedicated to the precomputation of the kernels $\{\Psi_{r,i}\}_{r,i}$ (for $1 \leq r \leq N$ and $1 \leq i \leq N$) and the constant term $\sum_{j=1} {A_r^{\mu_j}}^* s_{\mathcal{X}}^{\mu_j}$ involved in the computation of (14b) (see Appendix A.2), as well as the Lipschitz constant L_F of ∇F needed for setting the time steps τ and σ of Scheme (14) and ensuring its convergence towards a solution of (13) (see Appendix A.3). Algorithm 2 corresponds to the proposed source separation algorithm and performs the iterations of Scheme (14) in order to compute the (unmixed) target source images. Notice that each scheme iteration in Algorithm 2 only relies on FFT computations, yielding a loglinear complexity for this implementation of the numerical scheme.

Algorithm 1: `precomputations` module

Inputs: *a set of discrete 3D sinograms* $s_{\mathcal{X}} = (s_{\mathcal{X}}^{\mu_j})_{1\leq j\leq N_\mu}$, *with* $s_{\mathcal{X}}^{\mu_j} \in \mathbb{R}^{N_B\times N_{proj}}$ *(for* $1\leq j\leq N_\mu$*). The associated sequence of angles* $\mathcal{A} = \{(\theta_\ell,\varphi_\ell)\}_{1\leq\ell\leq N_{proj}}$ *parametrizing the magnetic field gradient orientations of the sinograms. A set of spectra* $h^d = (h^d_{i,j})$ *(*$1\leq i\leq N$, $1\leq j\leq N_\mu$*) such that* $h^d_{i,j}\in\mathbb{R}^{N_B}$ *corresponds to the spectrum of the* i*-th source* (X_i) *sampled using the same homogeneous magnetic field intensity nodes as the input sinogram* $s_{\mathcal{X}}^{\mu_j}$ *(see note*[a] *below).*

Output: *constant quantities needed in scheme* (14) *(those remain unchanged during all the scheme iterations).*

Core of the module:

`/* compute kernels` $(\Psi_{r,i})_{r,i}$ `(see Appendix A.2) */`

for $1\leq r\leq N$ *and* $1\leq i\leq N$ **do**

$$\Psi_{r,i} \leftarrow \sum_{j=1}^{N_\mu} \Psi_{r,i}^{\mu_j} \quad \texttt{// using (A.4) and an NFFT library}$$

$$\widehat{\Psi}_{r,i} \leftarrow \mathrm{DFT}(\Psi_{r,i})$$

$$\widehat{\Psi} \leftarrow \left(\widehat{\Psi}_{r,i}\right)_{\substack{1\leq r\leq N\\ 1\leq i\leq N}}$$

`/* compute a Lipschitz constant of` ∇F `(see Appendix A.3) */`

$$L_f \leftarrow \left(\max_{1\leq i\leq N}\sum_{r=1}^{N}\left\|\widehat{\Psi}_{r,i}\right\|_\infty^2\right)^{1/2}$$

`/* compute the constant offset term of (15) */`

for $1\leq r\leq N$ **do**

$$\Delta_r \leftarrow \sum_{j=1}^{N_\mu} A_r^{\mu_j *} s_{\mathcal{X}}^{\mu_j} \quad \texttt{// using [11, Algorithm 4]}$$

$$\Delta \leftarrow (\Delta_1,\Delta_2,\ldots,\Delta_N)$$

return $\left(\Delta, \widehat{\Psi}, L_f\right)$

[a] The spectra $h^d_{i,j}$ $(1\leq i\leq N,\ 1\leq j\leq N_\mu)$ used as inputs of this algorithm can be extracted from an EPR spectrum acquisition of the sample containing the mixture of species, using for instance EasySpin software [38], as explained in Section 4.1.

Algorithm 2: EPR source separation Algorithm

Inputs: *the same input set of sinograms $s_{\mathcal{X}}$, associated angles $\mathcal{A}$ and set of reference spectra h^d, as in Algorithm 1. A regularity parameter λ and a number of iterations n_{iter}.*

Output: *the reconstructed source images $u = (u_1, u_2, \ldots, u_N)$.*

Core of the module:

```
/* Precompute kernels, initialize scheme sequences and descent
 parameters */
```

$(\Delta, \widehat{\Psi}, L_f) \leftarrow \texttt{precomputations}(s_{\mathcal{X}}, h^d, \mathcal{A})$ `// see Algorithm 1`

for $1 \leq i \leq N$ **do**

- $u_i^0 \leftarrow 0_\Omega$ `// zero-valued image in` $\mathbb{R}^\Omega$
- $\overline{u}_i^0 \leftarrow 0_\Omega$ `// zero-valued image in` $\mathbb{R}^\Omega$
- $p_i^0 \leftarrow (0_\Omega, 0_\Omega, 0_\Omega)$ `// zero-valued signal in` $\mathbb{R}^\Omega \times \mathbb{R}^\Omega \times \mathbb{R}^\Omega$

$(\tau, \sigma) \leftarrow \left(\frac{1}{2L_f}, \frac{L_f}{12\lambda^2}\right)$

```
/* Main loop:  iterations of Scheme (14) */
```

for $0 \leq n < n_{iter}$ **do**

```
 // compute the N entries of ∇F(u^n)
```

- **for** $1 \leq r \leq N$ **do**
  - $\widehat{v}_r \leftarrow \sum_{i=1}^N \widehat{\Psi}_{r,i} \cdot \mathrm{DFT}(Zu_i^n)$ `//` Zu_i^n `is defined in (A.6)`
  - $v_r \leftarrow$ the restriction of $\mathrm{IDFT}(\widehat{v}_r)$ to Ω
  - $w_r \leftarrow v_r - \Delta_r$ `//` w_r `corresponds to the` r`-th entry of` $\nabla F(u^n)$
- $\texttt{gradF} \leftarrow (w_1, w_2, \ldots, w_N)$ `// this signal corresponds to` $\nabla F(u^n)$

```
 // perform one iteration of Scheme (14)
```

- $p^{n+1} \leftarrow \Pi(p^n + \sigma\lambda K\overline{u}^n)$ `// see (A.1) and Section 3.2`
- $u^{n+1} \leftarrow u^n - \tau\left(\texttt{gradF} + \lambda K^* p^{n+1}\right)$ `// see (A.2)`
- $\overline{u}^{n+1} \leftarrow 2\,u^{n+1} - u^n$

return u^{n+1}

Appendix B. Details of the information brought by the acquisition of multiple sinograms.

In this section, we provide mathematical insights about how the acquisition of multiple sinograms (with different field gradient intensities) instead of a single one simplifies the source separation task. For that purpose, let us focus on the separation of two sources X_1 and X_2 from two sinograms recorded at different gradient intensity μ_1 and $\mu_2 \neq \mu_1$. In the following, for any signal $f \in L^1(\mathbb{R}^n)$ (and any $n \geq 1$), we denote by $\mathcal{F}(f)$ the Fourier transform of f which is defined by

$$\forall \xi \in \mathbb{R}^N\,, \quad \mathcal{F}(f)(\xi) = \int_{\mathbb{R}^N} f(x) e^{-\imath\langle x,\xi\rangle} dx.$$

In presence of two species $\mathcal{X} = (X_1, X_2)$, the acquisition process described in (5) yields, for all $(B, \theta, \varphi) \in \mathbb{R}_+ \times [0, 2\pi] \times [0, \pi]$,

$$\left\{ \begin{array}{rcl} S_{\mathcal{X}}^{\mu_1}(B,\theta,\varphi) & = & \left(h_{X_1}^{\mu_1} * \mathcal{R}_{\theta,\varphi}(U_{X_1}) + h_{X_2}^{\mu_1} * \mathcal{R}_{\theta,\varphi}(U_{X_2})\right)(-B/\mu_1) \\ S_{\mathcal{X}}^{\mu_2}(B,\theta,\varphi) & = & \left(h_{X_1}^{\mu_2} * \mathcal{R}_{\theta,\varphi}(U_{X_1}) + h_{X_2}^{\mu_2} * \mathcal{R}_{\theta,\varphi}(U_{X_2})\right)(-B/\mu_2)\,. \end{array} \right. \tag{B.1}$$

In the following, let us set for all $(i, j) \in \{1, 2\}$ and for all $\xi \in \mathbb{R}$,

$$a_{i,j}(\xi) = \mathcal{F}(h_{X_i}^{\mu_j})(\xi) \quad \text{and} \quad Y_i^{\theta,\varphi}(\xi) = \mathcal{F}(\mathcal{R}_{\theta,\varphi}(U_{X_i}))(\xi)\,.$$

Then, taking the Fourier transform with respect to B of (B.1) at a given point $\xi \in \mathbb{R}$ yields

$$\left\{ \begin{array}{rcl} \mathcal{F}(S_{\mathcal{X}}^{\mu_1}(\cdot,\theta,\varphi))(\xi) & = & \mu_1(a_{1,1} \cdot Y_1^{\theta,\varphi})(-\mu_1\xi) + \mu_1(a_{2,1} \cdot Y_2^{\theta,\varphi})(-\mu_1\xi) \\ \mathcal{F}(S_{\mathcal{X}}^{\mu_2}(\cdot,\theta,\varphi))(\xi) & = & \mu_2(a_{1,2} \cdot Y_1^{\theta,\varphi})(-\mu_2\xi) + \mu_2(a_{2,2} \cdot Y_2^{\theta,\varphi})(-\mu_2\xi)\,. \end{array} \right. \tag{B.2}$$

Remarking that, for any $(i, j) \in \{1, 2\}^2$, we have

$$a_{i,j}(-\mu_j\xi) = \frac{1}{\mu_j}\,\mathcal{F}(h_{X_i})(\xi)\,,$$

and by setting $a_i(\xi) = \mathcal{F}(h_{X_i})(\xi)$ (for $i \in \{1, 2\}$), we get

$$\left\{ \begin{array}{rcl} \mathcal{F}(S_{\mathcal{X}}^{\mu_1}(\cdot,\theta,\varphi))(\xi) & = & a_1(\xi)\, Y_1^{\theta,\varphi}(-\mu_1\xi) + a_2(\xi)\, Y_2^{\theta,\varphi}(-\mu_1\xi) \\ \mathcal{F}(S_{\mathcal{X}}^{\mu_2}(\cdot,\theta,\varphi))(\xi) & = & a_1(\xi)\, Y_1^{\theta,\varphi}(-\mu_2\xi) + a_2(\xi)\, Y_2^{\theta,\varphi}(-\mu_2\xi)\,. \end{array} \right. \tag{B.3}$$

Rescaling in (B.3) the first equation by a factor $-\frac{1}{\mu_1}$ and the second one by a factor $-\frac{1}{\mu_2}$, we end up with, for any $\xi \in \mathbb{R}$,

$$\left\{ \begin{array}{rcl} \mathcal{F}(S_{\mathcal{X}}^{\mu_1}(\cdot,\theta,\varphi))(\frac{-\xi}{\mu_1}) & = & a_1(\frac{-\xi}{\mu_1})\, Y_1^{\theta,\varphi}(\xi) + a_2(\frac{-\xi}{\mu_1})\, Y_2^{\theta,\varphi}(\xi) \\ \mathcal{F}(S_{\mathcal{X}}^{\mu_2}(\cdot,\theta,\varphi))(\frac{-\xi}{\mu_2}) & = & a_1(\frac{-\xi}{\mu_2})\, Y_1^{\theta,\varphi}(\xi) + a_2(\frac{-\xi}{\mu_2})\, Y_2^{\theta,\varphi}(\xi)\,. \end{array} \right. \tag{B.4}$$

Therefore, for each frequency value $\xi \in \mathbb{R}$, (B.4) corresponds to linear a system made of two equations and two unknowns $(Y_1^{\theta,\varphi}(\xi), Y_2^{\theta,\varphi}(\xi))$. We recall that thanks to Slice Central Theorem, we have

$$Y_1^{\theta,\varphi}(\xi) = \mathcal{F}(U_{X_1})(\xi e_{(\theta,\varphi)}) \quad \text{and} \quad Y_2^{\theta,\varphi}(\xi) = \mathcal{F}(U_{X_2})(\xi e_{(\theta,\varphi)})\,,$$

so that solving (B.4) for any ξ would provide the Fourier coefficients of the source images (and thus, the two source images after inverse Fourier transformation).

Considering a dataset made of only one sinogram acquisition amounts to removing one row from System (B.4), leading to an ill-posed problem. Although we illustrated that the use of TV regularization in the inversion process can lead to successful separation when the two species to separate are spectrally distant enough, we also showed that the separation from one sinogram fails when the two species exhibit similar EPR signals. In that situation, the use of a second sinogram can make the system (B.4) well-posed and the separation possible (although TV-regularization remains necessary during the inversion process in order to correctly handle the noise corrupting the measurements).

Appendix C. TAM and DPPH spectra extraction for the dataset presented in Figure 11

We provide in Figure C.14 the results of the extraction of TAM and DPPH spectra from the two measured spectra $(h_{\mathcal{X}}^{(1)}, h_{\mathcal{X}}^{(2)})$ of their mixture presented in Figure 11 (see also Figure 12 for a close-up view). The set of spectra $(h_{\mathcal{X}}^{(1)}, h_{\mathcal{X}}^{(2)})$ was processed as a whole using EasySpin to perform the fitting of those measurements using TAM and DPPH molecular systems. We configured the fitting process to take into account possible shifts and intensity rescaling between $h_{\mathcal{X}}^{(1)}$ and $h_{\mathcal{X}}^{(2)}$. We end up with two spectra of TAM and DPPH that are both consistent with the acquisition $h_{\mathcal{X}}^{(1)}$ (first

row of Figure C.14) and two spectra of TAM and DPPH that are both consistent with the acquisition $h_{\mathcal{X}}^{(2)}$ (second row of Figure C.14). Consistency of the spectra with respect to the species is also guaranteed by our extraction procedure. Indeed, both extracted TAM spectra (left column) exhibit the same peak to peak linewidth (here 0.3 G) and similarly for the extracted DPPH spectra (right column) with a peak to peak linewidth equal to 0.95 G.

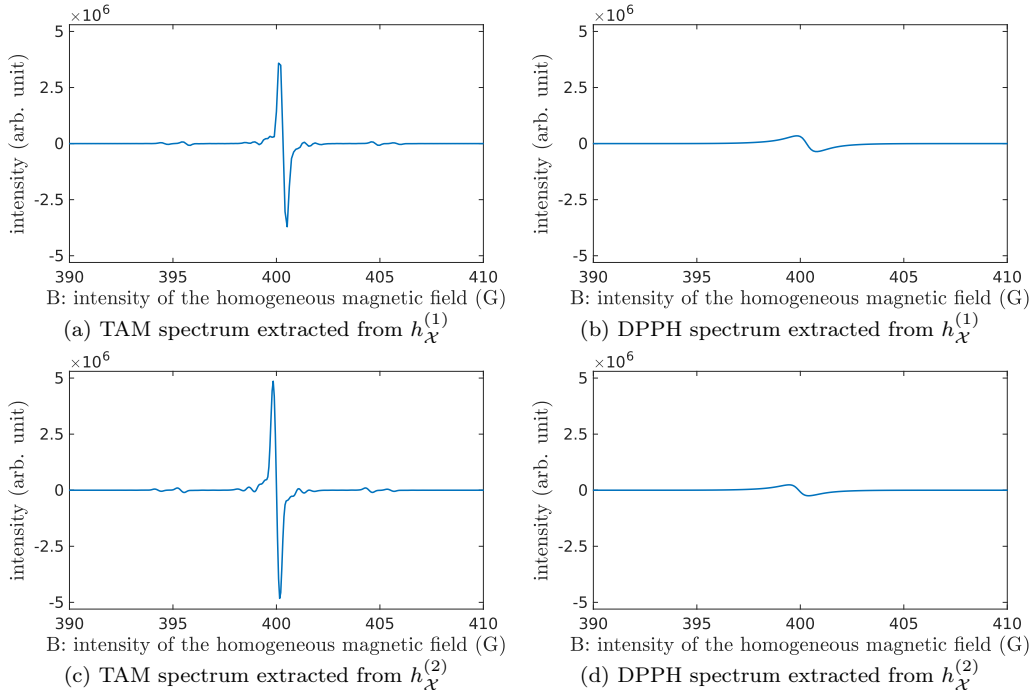

(a) TAM spectrum extracted from $h_{\mathcal{X}}^{(1)}$

(b) DPPH spectrum extracted from $h_{\mathcal{X}}^{(1)}$

(c) TAM spectrum extracted from $h_{\mathcal{X}}^{(2)}$

(d) DPPH spectrum extracted from $h_{\mathcal{X}}^{(2)}$

Figure C.14: **EasySpin extraction of TAM and DPPH spectra from two EPR spectra of their mixture. First row**: spectra of TAM and DPPH being consistent with the acquisition $h_{\mathcal{X}}^{(1)}$, in the sense that $(a)+(b) \approx h_{\mathcal{X}}^{(1)}$. **Second row**: spectra of TAM and DPPH being consistent with the acquisition $h_{\mathcal{X}}^{(2)}$, in the sense that $(c)+(d) \approx h_{\mathcal{X}}^{(2)}$. The displayed sweep-width was reduced to the range $B \in [390, 410]$ (G) to improve the display.

There is certainly room for improvement in this spectra separation process, notably around the inner carbon signal of TAM which deviates from the experimental one.

Declaration of interests

The authors declare that they have no known competing financial interests or personal relationships that could have appeared to influence the work reported in this paper.

Acknowledgements

The authors acknowledge Dr Raffaella Soleti from the EPR facility of the SFR ICAT University of Angers for assistance.

References

[1] L. J. Berliner, H. Fujii, Magnetic resonance imaging of biological specimens by electron paramagnetic resonance of nitroxide spin labels, Science 227 (4686) (1985) 517–519. doi:10.1126/science.2981437.

[2] P. Kuppusamy, P. Wang, J. L. Zweier, M. C. Krishna, J. B. Mitchell, L. Ma, C. E. Trimble, C. J. C. Hsia, Electron paramagnetic resonance imaging of rat heart with nitroxide and polynitroxyl-albumin, Biochemistry 35 (22) (1996) 7051–7057. doi:10.1021/bi952857s.

[3] E. Martyna, R. Bell, D. Hleihel, E. D. Barth, C. McFaul, C. R. Haney, J. Bielanska, K. Pustelny, K.-H. Ahn, C. A. Pelizzari, M. Kocherginsky, H. J. Halpern, Electron paramagnetic resonance oxygen image hypoxic fraction plus radiation dose strongly correlates with tumor cure in fsa fibrosarcomas, International Journal of Radiation Oncology Biology Physics 71 (2) (2008) 542–549. doi:10.1016/j.ijrobp.2008.02.022.

[4] B. Gallez, Oxygenation status in normal tissues, pathological tissues and malignant tumors: A p o2 database based on electron paramagnetic resonance (epr) oximetry measurements, Applied Magnetic Resonance 52 (10) (2021) 1395–1450.

[5] M. Sathiya, J.-B. Leriche, E. Salager, D. Gourier, J.-M. Tarascon, H. Vezin, Electron paramagnetic resonance imaging for real-time monitoring of li-ion batteries, Nature communications 6 (2015). doi:10.1038/ncomms7276.

[6] M. Abou Fadel, X. Zhang, A. De Juan, R. Tauler, H. Vezin, L. Duponchel, Extraction of pure spectral signatures and corresponding chemical maps from epr imaging data sets: Identifying defects on a caf 2 surface due to a laser beam exposure, Analytical chemistry 87 (2015) 3929–3935. doi:10.1021/ac504733u.

[7] L. Binet, D. Gourier, S. Derenne, Potential of epr imaging to detect traces of primitive life in sedimentary rocks, Earth and Planetary Science Letters 273 (2008) 359–366. doi:10.1016/j.epsl.2008.06.052.

[8] D. Johnson, R. Ahmad, G. He, A. Samouilov, J. Zweier, Compressed sensing of spatial electron paramagnetic resonance imaging, Magnetic Resonance in Medecine 72 (3) (2014) 893–901. doi:10.1002/mrm.24966.

[9] S. Durand, Y.-M. Frapart, M. Kerebel, Electron paramagnetic resonance image reconstruction with total variation and curvelets regularization, Inverse Problems 33 (11) (2017) 114002. doi:10.1088/1361-6420/aa8412.

[10] M. Kerebel, Méthodes variationnelles pour l'imagerie en résonance paramagnétique électronique, Thesis, https://theses.hal.science/tel-02122784 (2017).

[11] R. Abergel, M. Boussâa, S. Durand, Y.-M. Frapart, Electron Paramagnetic Resonance Image Reconstruction with Total Variation Regularization, Image Processing On Line 13 (2023) 90–139. doi:10.5201/ipol.2023.414.

[12] S. Som, L. C. Potter, R. Ahmad, P. Kuppusamy, A parametric approach to spectral–spatial epr imaging, Journal of Magnetic Resonance 186 (1) (2007) 1–10. doi:10.1016/j.jmr.2006.12.018.

[13] R. Nakaoka, K. Kato, K. Yamamoto, H. Yasui, S. Matsumoto, I. A. Kirilyuk, V. V. Khramtsov, O. Inanami, H. Hirata, Electron paramagnetic resonance implemented with multiple harmonic detections successfully maps extracellular ph in vivo, Analytical Chemistry 95 (8) (2023) 3940–3950. doi:10.1021/acs.analchem.2c03194.

[14] D. A. Komarov, A. Samouilov, H. Hirata, J. L. Zweier, High fidelity triangular sweep of the magnetic field for millisecond scan epr imaging,

Journal of Magnetic Resonance 329 (2021) 107024. doi:https://doi.org/10.1016/j.jmr.2021.107024.

[15] K.-H. Ahn, H. J. Halpern, Spatially uniform sampling in 4-d epr spectral-spatial imaging, Journal of Magnetic Resonance 185 (1) (2007) 152–158. doi:https://doi.org/10.1016/j.jmr.2006.12.007.

[16] M. Hoch, A. Day, Imaging of paramagnetic centres in diamond, Solid State Communications 30 (4) (1979) 211–213. doi:10.1016/0038-1098(79)90336-3.

[17] B. B. Williams, X. Pan, H. J. Halpern, Epr imaging: The relationship between cw spectra acquired from an extended sample subjected to fixed stepped gradients and the radon transform of the resonance density, Journal of Magnetic Resonance 174 (1) (2005) 88–96. doi:10.1016/j.jmr.2005.01.003.

[18] B. B. Williams, K. Ichikawa, C.-M. Kao, H. Halpem, X. Pan, Deblurring and noise suppression in spatial epr imaging, in: 2002 IEEE Nuclear Science Symposium Conference Record, Vol. 3, 2002, pp. 1602–1606. doi:10.1109/NSSMIC.2002.1239629.

[19] G. Redler, Z. Qiao, B. Epel, H. J. Halpern, Real-time image reconstruction for pulse epr oxygen imaging using a gpu and lookup table parameter fitting, Concepts in Magnetic Resonance Part B: Magnetic Resonance Engineering 45 (1) (2015) 46–57. doi:10.1002/cmr.b.21281.

[20] F. Geng, Q. Yang, C. Li, M. Shen, Q. Chen, B. Hu, Mapping the distribution and the microstructural dimensions of metallic lithium deposits in an anode-free battery by in situ epr imaging, Chemistry of Materials 33 (21) (2021) 8223–8234. doi:10.1021/acs.chemmater.1c02323.

[21] Z. Qiao, D. Liang, S. Tang, H. Halpern, Optimization-based image reconstruction from fast-scanned, noisy projections in epr imaging, IEEE Access 7 (2019) 19590–19601. doi:10.1109/ACCESS.2019.2897140.

[22] K. Kimura, N. Iguchi, H. Nakano, H. Yasui, S. Matsumoto, O. Inanami, H. Hirata, Redox-sensitive mapping of a mouse tumor model using sparse projection sampling of electron paramagnetic resonance, Antioxidants & Redox Signaling 36 (1-3) (2022) 57–69. doi:10.1089/ars.2021.0003.

[23] K.-i. Matsumoto, T. Yahiro, K.-i. Yamada, H. Utsumi, In vivo epr spectroscopic imaging for a liposomal drug delivery system, Magnetic Resonance in Medicine 53 (5) (2005) 1158–1165. doi:10.1002/mrm.20460.

[24] M. C. Krishna, S. Matsumoto, H. Yasui, K. Saito, N. Devasahayam, S. Subramanian, J. B. Mitchell, Electron Paramagnetic Resonance Imaging of Tumor pO2, Radiation Research 177 (4) (2012) 376–386. doi:10.1667/RR2622.1.

[25] P. Kuppusamy, M. Chzhan, K. Vij, M. Shteynbuk, D. J. Lefer, E. Giannella, J. L. Zweier, Three-dimensional spectral-spatial epr imaging of free radicals in the heart: a technique for imaging tissue metabolism and oxygenation., Proceedings of the National Academy of Sciences 91 (8) (1994) 3388–3392. doi:10.1073/pnas.91.8.3388.

[26] G. Redler, B. Epel, H. J. Halpern, Maximally spaced projection sequencing in electron paramagnetic resonance imaging, Concepts in Magnetic Resonance Part B: Magnetic Resonance Engineering 45 (1) (2015) 33–45. doi:10.1002/cmr.b.21280.

[27] Z. Zhang, B. Epel, B. Chen, D. Xia, E. Y. Sidky, Z. Qiao, H. Halpern, X. Pan, 4d-image reconstruction directly from limited-angular-range data in continuous-wave electron paramagnetic resonance imaging, Journal of Magnetic Resonance 350 (2023) 107432. doi:10.1016/j.jmr.2023.107432.

[28] L. Condat, D. Kitahara, A. Contreras, A. Hirabayashi, Proximal splitting algorithms for convex optimization: A tour of recent advances, with new twists, SIAM Review 65 (2) (2023) 375–435. doi:10.1137/20M1379344.

[29] L. Condat, A primal–dual splitting method for convex optimization involving lipschitzian, proximable and linear composite terms, Journal of Optimization Theory and Applications 158 (2013). doi:10.1007/s10957-012-0245-9.

[30] A. Chambolle, T. Pock, On the ergodic convergence rates of a first-order primal–dual algorithm, Mathematical Programming 159 (2015). doi:10.1007/s10107-015-0957-3.

[31] Y. Drori, S. Sabach, M. Teboulle, A simple algorithm for a class of nonsmooth convex–concave saddle-point problems, Operations Research Letters 43 (2) (2015) 209–214. doi:10.1016/j.orl.2015.02.001.

[32] B. C. Vũ, A splitting algorithm for dual monotone inclusions involving cocoercive operators, Advances in Computational Mathematics 38 (3) (2013) 667–681. doi:10.1007/s10444-011-9254-8.

[33] M. Frigo, S. G. Johnson, The design and implementation of FFTW3, Proceedings of the IEEE 93 (2) (2005) 216–231. doi:10.1109/JPROC.2004.840301.

[34] H. H. Bauschke, P. L. Combettes, Convex analysis and monotone operator theory in hilbert spaces, in: CMS Books in Mathematics, 2011. URL https://api.semanticscholar.org/CorpusID:117838286

[35] I. Ekeland, R. Témam, Convex Analysis and Variational Problems, Society for Industrial and Applied Mathematics, 1999. doi:10.1137/1.9781611971088.

[36] R. Ahmad, Y. Deng, D. S. Vikram, B. Clymer, P. Srinivasan, J. L. Zweier, P. Kuppusamy, Quasi monte carlo-based isotropic distribution of gradient directions for improved reconstruction quality of 3d epr imaging, Journal of Magnetic Resonance 184 (2) (2007) 236–245. doi:10.1016/j.jmr.2006.10.008.

[37] I. Dhimitruka, M. Velayutham, A. A. Bobko, V. V. Khramtsov, F. A. Villamena, C. M. Hadad, J. L. Zweier, Large-scale synthesis of a persistent trityl radical for use in biomedical epr applications and imaging, Bioorganic & Medicinal Chemistry Letters 17 (24) (2007) 6801–6805. doi:10.1016/j.bmcl.2007.10.030.

[38] S. Stoll, A. Schweiger, EasySpin, a comprehensive software package for spectral simulation and analysis in EPR, Journal of Magnetic Resonance 178 (1) (2006) 42–55. doi:10.1016/j.jmr.2005.08.013.

[39] T. D. Gluth, M. Poncelet, M. Gencheva, E. H. Hoblitzell, V. V. Khramtsov, T. D. Eubank, B. Driesschaert, Biocompatible monophosphonated trityl spin probe, hope71, for in vivo measurement of po2, ph, and [pi] by electron paramagnetic resonance spectroscopy, Analytical Chemistry 95 (2) 946–954. doi:10.1021/acs.analchem.2c03476.

[40] S. D'Alessandro, B. Posocco, A. Costa, G. Zahariou, F. Lo Schiavo, D. Carbonera, M. Zottini, Limits in the use of cptio as nitric oxide scavenger and epr probe in plant cells and seedlings, Frontiers in Plant Science 4 (2013). doi:10.3389/fpls.2013.00340.

[41] J. Keiner, S. Kunis, D. Potts, Using NFFT 3—A Software Library for Various Nonequispaced Fast Fourier Transforms, ACM Transactions on Mathematical Software 36 (4) (2009). doi:10.1145/1555386.1555388.